Heterogeneous Domain Decomposition for Computational Aeroacoustics

J. Utzmann,* T. Schwartzkopff,† M. Dumbser,† and C.-D. Munz‡
University of Stuttgart, 70550 Stuttgart, Germany

This paper presents a strategy to accelerate the direct simulation of aeroacoustic problems in terms of CPU time. The key idea is to introduce a heterogeneous domain decomposition. The whole computational domain is subdivided into smaller domains. In each of these subdomains the equations, the discretization, the mesh, and the time step may be different and are adapted to the local behavior of the solution. To reduce the total number of elements we propose the use of high order methods. Here the class of arbitrary high-order using derivatives–finite volume schemes on structured meshes and arbitrary high-order using derivatives discontinuous Galerkin methods on unstructured meshes seem a good choice to us. The coupling procedure is validated and numerical results for the interface transmission problem and the single airfoil gust response problem (from *4th Computational Aeroacoustics Workshop on Benchmark Problems*, CP-2004 212954, NASA, 2004) are presented, together with the acoustic scattering problem at a cylinder and at multiple objects. The coupling approach proves to be especially efficient for the propagation of sound in large domains.

Nomenclature

A, B, C	=	Jacobi matrices
A_{domain}	=	domain area
c_0	=	background speed of sound
F	=	flux function
f_{CPU}	=	clock frequency of the processor
k	=	wave number
$\mathcal{L}(f, g)$	=	original Leibniz rule operator for two scalar functions f and g
$\mathcal{L}(X_i)$	=	Lagrange interpolation onto coordinate X_i of Gauss integration point i
$\mathcal{L}_*(f, g)$	=	original Leibniz rule operator without the last term in the sum
$\mathcal{L}_{**}(fg, f, g)$	=	modified Leibniz rule operator
L_1, L_2, L_∞	=	error norms
Ma_∞	=	ambient Mach number
N_G	=	mesh size ratio
$N_{\text{processors}}$	=	number of processors
$\boldsymbol{n}$	=	normal vector
$\mathcal{O}$	=	order of accuracy
p, p_0, p'	=	pressure, background pressure, pressure perturbation
r	=	flux parameter
S	=	estimation of largest wave speeds
s_i, s_t, s_r	=	distances along cut sections (incident, transmitted, and reflected wave)
t_{CPU}, t_{end}, t_{factor}	=	CPU time, end time of calculation, time factor
$\boldsymbol{U}$, $\boldsymbol{U}_0$, $\boldsymbol{U}'$	=	state vector, background state vector, perturbation state vector
$\bar{U}$	=	integral mean value of the state vector
U_{GP_i}	=	state vector at the position of Gauss integration point i
u, u_0, u'	=	velocity, background velocity, velocity perturbation in x direction
V, V_{S_i}	=	volume of ghost cell, projection of ghost cell
v, v_0, v'	=	velocity, background velocity, velocity perturbation in y direction
Γ	=	domain interface
γ	=	adiabatic exponent
Δt	=	time step
Δx, Δy	=	grid spacing in x and y direction
λ	=	wavelength of acoustic waves
ϵ	=	camber ratio
Θ	=	angle of incidence
ρ, ρ_0, ρ'	=	density, background density, density perturbation
τ	=	time parameter for Taylor expansion
Ω	=	domain
ω	=	angular frequency
ω_i	=	Gauss weight of Gauss integration point i

Subscripts

E, LE	=	nonlinear Euler domain, linearized Euler domain
F, G	=	fine-grid domain, coarse-grid domain
i, j, k	=	index parameters
L, R	=	left side and right side of the interface

*Dipl.-Ing., Ph.D. Student, Institut für Aerodynamik und Gasdynamik, Pfaffenwaldring 21. Member AIAA.
†Dr.-Ing., Institut für Aerodynamik und Gasdynamik, Pfaffenwaldring 21.
‡Professor Dr., Institut für Aerodynamik und Gasdynamik, Pfaffenwaldring 21. Member AIAA.
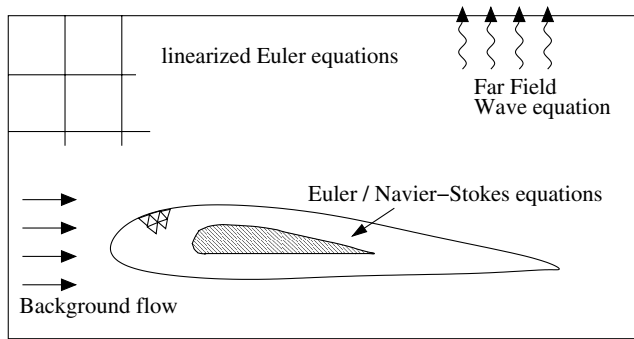
I.   Introduction

THE field of computational aeroacoustics (CAA) is very demanding for two main reasons: the requirements regarding the accuracy of the methods are very high and in general, quite large domains have to be computed. It was Lighthill who developed the first acoustic analogy [1] and started the field of noise predictions. In the following years, the acoustic analogies have been continuously improved. However, these methods suer from basic problems: First of all, there is no feedback from acoustics to the fluid flow. Furthermore, all of these analogies model the acoustic sources in some way, implying an uncertainty in the modeling.

The method that is proposed here does not suffer from these problems, as it is basically a direct simulation. However, an accurate and feasible direct simulation that considers both the generation of sound and its propagation into the far field is hard to realize with one

Fig. 1   Sketch of nonoverlapping domain decomposition.

numerical method in a single computational domain. The idea is to use a nonoverlapping domain decomposition method where the equations, methods, grids, and time steps are adapted to meet the local requirements. Such a decomposition has already been proposed for jet noise by Freund et al. [2] Also composite overset structured grids are related to the presented domain decomposition. Chimera methods (introduced by Steger et al. [3]) couple structured body-fitted grid components with Cartesian background grids and are used in a wide range of applications. An overview is given by Meakin [4]. However, these approaches did not simplify the domains to the degree that is described here.

The outline of the paper is the following: First we start with a short description of the basic problems of CAA. Then we briefly introduce the high order methods for structured and unstructured grids. In Sec. IV, the domain decomposition method is described and analyzed, for example, regarding the order of convergence. In the last section several numerical examples are given.

II.   Basic Problems

The basic problems in computational aeroacoustics are briefly described. We start at the pure physical problem with no numerics involved. In principle, the complete problem can be described by the full nonlinear compressible Navier–Stokes equations. However, it is not necessary to include all physical effects in the whole domain. There are three different areas in the domain of interest (see Fig. 1). The area around bodies or interfaces include all nonlinear as well as viscous effects. A short distance away, the viscous parts may already be neglected and the simpler system of nonlinear Euler equations can be used. Further away, nonlinear effects become less important and the linearized Euler equations become a good choice. This is a region where only small perturbations, for example, acoustics, propagate.

Next we want to look at the multiscale problem in aeroacoustics. The interesting acoustic wavelength is often much larger than the length scale of the fluid flow phenomena that generate the wave. These phenomena are eddies that have a much smaller structure. On the other hand, eddies are advected with the fluid flow, whereas acoustic waves run with the speed of sound.

Last but not least we want to look at the numerics. In the vicinity of complex obstacles one has two major choices in discretizing the domain. First, one can use body-fitted block-structured meshes and second one can use completely unstructured meshes. We will use fully unstructured meshes because complex geometries can be handled much more easily by these grids. On the other hand, there is no need to use these meshes away from the bodies where everything is regular. Here it is much more convenient to use structured,

Cartesian uniformly spaced meshes for the following reasons: they need much less memory, can be implemented much more effectively, and the step to high order is much easier.

The idea of the decomposition method is now to simplify everything as much as possible. This means that the equations that are used are adapted to the relevant local phenomena. The grids and, due to the CFL condition, the time steps are chosen as large as possible and also the type of grid is flexible. The complete setup of this method is described in Sec. IV.

III.   Numerical Methods

A key ingredient in our method is to use high order schemes everywhere. The recent idea of arbitrary high-order using derivatives (ADER) schemes by Toro et al. [5–7] has been adopted and optimized for linear and nonlinear equations on structured grids in the framework of finite volume (FV) schemes by Schwartzkopff et al. [8–11]. The same idea is used for the discontinuous Galerkin (DG) methods by Dumbser et al. [12–14] that is used on unstructured grids. A direct comparison of these method is given in Table 1. The main advantage of the ADER–FV schemes on structured grids is that the first step in a FV scheme, the reconstruction, becomes rather simple, as all neighborhoods are known directly. Hence, the implementation of higher order becomes easier. The advantage of DG methods is that they are very local as they only need direct neighbors, thus high order on unstructured meshes can be achieved easily.

IV.   Heterogeneous Domain Decomposition

The aim of the present work was to develop a method that makes it possible to calculate a direct simulation of an aeroacoustic problem within reasonable time. The domain of the calculation shall cover both the area of sound generation and the area of sound propagation into the far field. Hence, the main goal was to reduce the effort by a domain decomposition method.

First of all, unstructured grids are used only in the direct vicinity of complex bodies. As fast as possible, these grids are aligned to a straight line and are switched to structured, Cartesian meshes.

Second, we allow the cell size to jump at a domain interface. Thus, the mesh can be adapted to the local flow phenomena, which means that the eddies in the flow around a body need not be resolved in the near far field, where one is only interested in the acoustics and therefore the grid size may be much larger. The numerical methods used are always explicit time integration methods with a time step that is chosen as large as possible in each domain. As a consequence, not only the spatial grid size has a jump at an interface, but also the time step. By this, the far-field domains are updated only once in a while because large regions are covered with only a small number of cells.

Finally, we allow the underlying equations to change. The nonlinear equations are used in the core regions near sound generating obstacles or phenomena and for the surrounding area we solve only the linearized equations. For the linearized equations, the underlying method can be optimized very well, see Schwartzkopff [10]. By using these techniques, the decrease of memory and CPU time becomes immense and a direct simulation in this sense becomes more and more feasible. In the following paragraphs we explain some basic parts and properties of these methods.

Table 1   Comparison of finite volume and discontinuous Galerkin methods

	FV methods		DG methods
+	Easy to implement	−	Difficult to implement
+	High order on regular, structured grids	−	Slow
+	Fast algorithms for structured grids	+	Efficient parallelization
−	High order on unstructured grids is difficult	+	High order on unstructured grids is easy
−	Unstructured grid must be regular	+	High convergence rates on irregular grids

A. Coupling Strategies

1. Coupling of Different Equations

a. Physical Considerations. The coupling of different equations is indeed a very demanding issue. The coupling of nonlinear and linear Euler equations has been discussed by Schwartzkopff et al. [15,16]. If a conservative coupling regarding the flux at the interface is used, the reflection errors can be estimated easily. The propagation speed of the wave changes from $u + \sqrt{\gamma p/\rho}$ to the linear speed $u_0 + \sqrt{\gamma p_0/\rho_0}$. Therefore, the interface Γ can be interpreted as an artificially introduced material interface of two materials with different wave speeds. For this case, the physics of waves [17] directly gives estimates for reflections r with the refraction indices n and the refraction for a wave front with the angle of incidence α^E:

$$n^{\mathrm{LE}} = \frac{1}{u_0 + c_0}, \qquad n^E = \frac{1}{u + c} \tag{1}$$

$$r = \left(\frac{n^{\mathrm{LE}} - n^E}{n^{\mathrm{LE}} + n^E}\right)^2 \approx \left(\frac{u' + \mathcal{O}(c')}{2\mathcal{O}(u_0) + 2\mathcal{O}(c_0)}\right)^2 \tag{2}$$

$$\alpha^{\mathrm{LE}} = \arcsin\left(\frac{n^E}{n^{\mathrm{LE}}}\sin(\alpha^E)\right) \tag{3}$$

Even total reflection is possible if the product $n^E/n^{\mathrm{LE}} \cdot \sin(\alpha^E)$ gets larger than 1, which corresponds to

$$\sin(\alpha^E) = \frac{n^{\mathrm{LE}}}{n^E} \approx \frac{u_0 + \mathcal{O}(c_0)}{u_0 + c_0} + \frac{u' + \mathcal{O}(c')}{u_0 + c_0} \tag{4}$$

For example, if the perturbations U' of the state vector are 10% of the U_0, then the angle for total reflection will be $\alpha^E \approx 64$ deg.

One can conclude that if a numerical coupling scheme is applied that simulates the artificially introduced interface like a material interface using the continuity of the flux, then there will certainly be reflections at the interface that are of the magnitude $\mathcal{O}(U'^2)$. The aim is now to find a transmission condition that avoids this behavior at the artificial interface.

b. Numerical Interface Treatment. It is possible to reduce these reflections only, if fluxes are defined at the interface that may be discontinuous. We do not look for a globally weak solution, but for a solution that is as continuous as possible. An obvious idea is to combine the different mathematical models into one, so that it can be handled in an easier way. Therefore, a new variable r is introduced and a new flux function

$$F_r^{\star}(U) = \frac{1 + r}{2} F^E(U) + \frac{1 - r}{2} F^{\mathrm{LE}}(U) \tag{5}$$

is generated, which is now valid in Ω_E ($r = +1$) and Ω_{LE} ($r = -1$). The discontinuity in the flux function is shifted to the variable r. This allows one to define a Jacobian matrix of the flux in the whole domain in order to calculate the eigenvalues at the interface and to define the flux of a FV scheme. In the following, we use the flux of the Harten, Lax, and van Leer (HLL) scheme (see Schwartzkopff et al. [15,16] for details).

c. Numerical Tests. To test the interface condition, a Gaussian pressure pulse is prescribed in the initial condition. The amplitude of the pulse is $\hat{p}' = 0.1 \cdot p_0$. This pulse will break down into two parts, one moving to the left and leaving the domain and the other one moving to the right and passing the interface from $\Omega^E \leftrightarrow \Omega^{\mathrm{LE}}$ (see Fig. 3). The test is carried out using an equal spatial discretization and time step. An analysis for varying time steps and different grids has also been done by Schwartzkopff [16] and leads to very similar results.

d. Smooth Variation of the Interface Flux. So far, nothing has been said about how to choose r at the interface. There are two natural possibilities. The function r jumps at the interface from $r = 1$ to $r = -1$. The other idea is to use a smooth variation of r that corresponds to a smooth variation from nonlinear equations to linearized Euler equations. The hope is that the reflections at a smeared interface

are much smaller. The parameter r is chosen such that it varies from $r = +1$ to $r = -1$ with a cos function, spread over 40 cells. Figure 4 gives a comparison of the reflections produced by this condition compared with reflections produced by the discontinuous switch. Note that this reflection is indeed of the order $\mathcal{O}(U'^2)$ as predicted by Eq. (2). For the continuous switch, it can be seen clearly that the amplitude of the reflection has been decreased by about $\frac{1}{3}$. Unfortunately, the spatial stretch has been grown by the same amount. Thus, the integral over the reflection is more or less the same. Therefore, the smooth variation does not generate an interface condition that is suitable for this problem.

e. Discontinuous Interface Flux. In this approach, different r^E and r^{LE} distributions are used at the interface. These distributions are sketched in Fig. 2. The fluxes at the interface Γ are

$$F_{\partial\Omega_E \cap \Gamma} = F^{\mathrm{HLL}}[F_{r=1}^{\star}(U_L), F_{r=0}^{\star}(U_R)] \tag{6}$$

$$F_{\partial\Omega_{\mathrm{LE}} \cap \Gamma} = F^{\mathrm{HLL}}[F_{r=0}^{\star}(U_L), F_{r=-1}^{\star}(U_R)] \tag{7}$$

This definition clearly leads to a flux difference $F_{\partial\Omega_E \cap \Gamma} - F_{\partial\Omega_{\mathrm{LE}} \cap \Gamma}$ at the interface and thus this scheme is not conservative at the interface. The flux difference can be written down explicitly for the HLL scheme, assuming subsonic conditions:

$$\Delta F_{\Gamma} = \frac{S_R}{S_R - S_L}\frac{1}{2}(F_L^E - F_L^{\mathrm{LE}}) - \frac{S_L}{S_R - S_L}\frac{1}{2}(F_R^E - F_R^{\mathrm{LE}}) \tag{8}$$

where S_L and S_R are an estimation of the largest wave speeds to the left and to the right, respectively. The numerical results for a pulse passing the interface from Ω^E to Ω^{LE} can be found in Fig. 5 and for a pulse in the other direction in Fig. 6. The reflections with this new condition are compared with the reflections that are generated by the
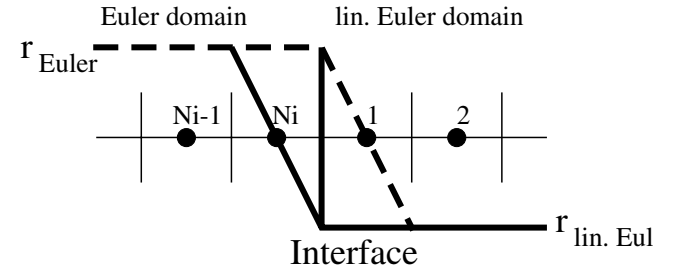

Fig. 2 Sketch of r^E and r^{LE} distributions used to produce an nonconservative interface flux.
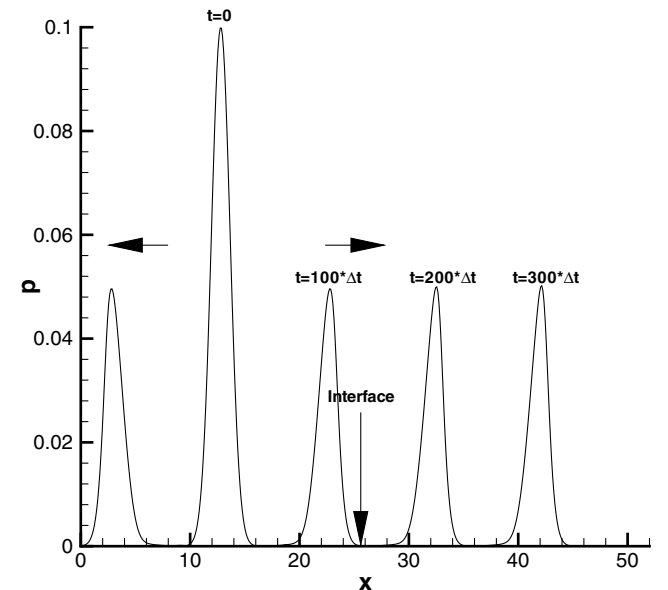

Fig. 3 Evolution of a Gaussian pressure pulse as initial condition.
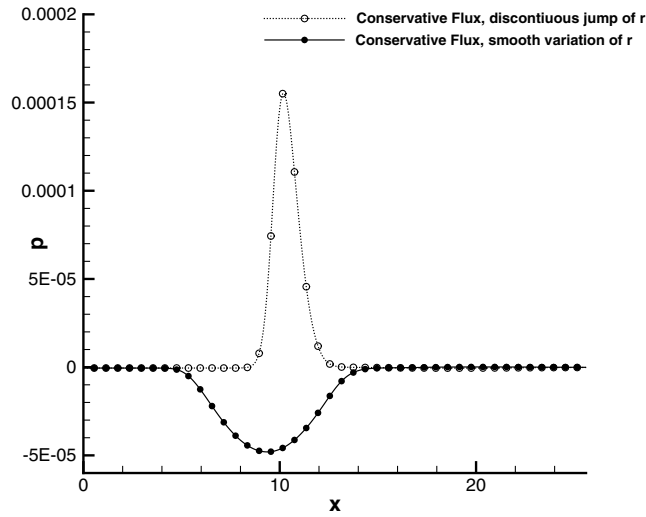
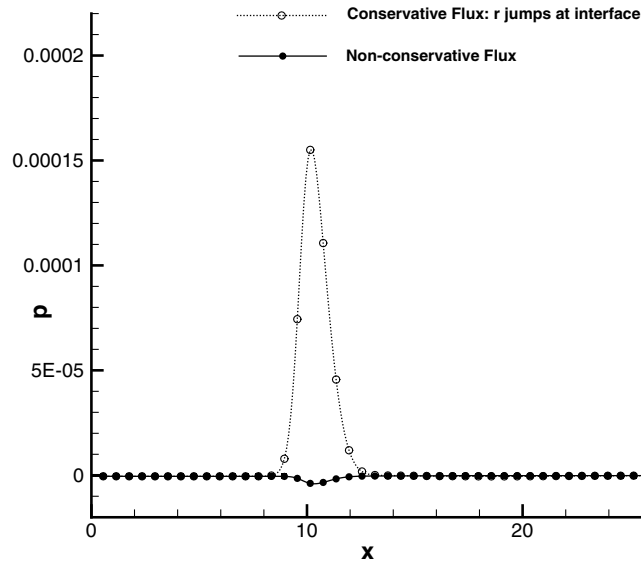**Fig. 4 Conservative interface flux: smooth variation and jump of *r*.**

Fig. 5 Conservative flux vs nonconservative flux at the interface: $\Omega^E \rightarrow \Omega^{LE}$.
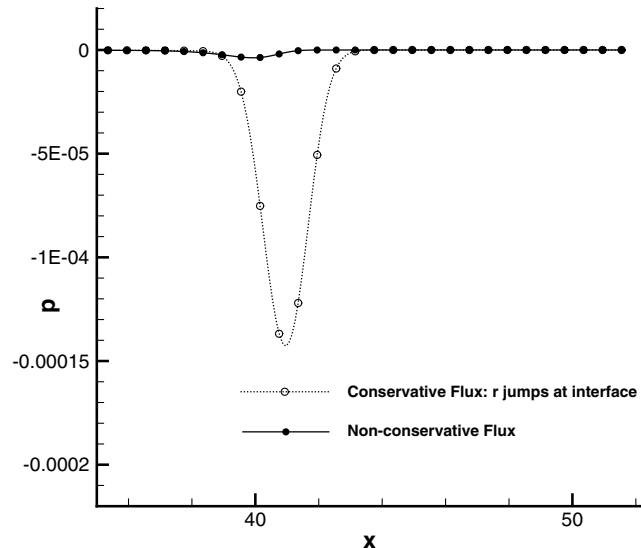

Fig. 6 Conservative flux vs nonconservative flux at the interface: $\Omega^{LE} \rightarrow \Omega^E$.

discontinuous switch. It can be seen very clearly that the amplitude of the reflections have been decreased drastically with this new interface flux and that the reduction rate is of about 2 orders of magnitude. Furthermore, the reflection predicted by Eq. (2) has been validated. A rigorous analysis in one and two dimensions is the subject of current work. The further results of this paper were calculated using the discontinuous flux approach. Then, the whole coupling procedure is based only on the exchange of the states.

2. Coupling of Different Grids

Two different domains Ω_1 and Ω_2 are coupled at their common boundary $\partial\Omega = \Gamma$ only over data in the so-called ghost cells. These ghost cells are then used by the numerical method to update the inner cells in each domain. The number of ghost cells that are needed for the numerical method depends strongly on the method itself. The DG methods are very local and so they need only one row of ghost cells where the high order ADER–FV schemes use reconstruction operators and thus need a larger number of ghost cells.

a. Fully Conservative Coupling. Two cases may occur in the coupling procedure:

1) Restrictions: The projection of the ghost cell on the partner domain covers more than one cell (see left picture in Fig. 7). In this case an integral average of all cells that lie partially in the projection is used. The weight of this averaging is the ratio of the respective area of cell V_{S_i} which is in the projection and the total area of the ghost cell V:

$$\bar{U}^{\Omega_G} = \frac{1}{V}\sum_i V_{S_i} \bar{U}_i^{\Omega_F} \qquad (9)$$

As it is obvious from Fig. 8, very complex and small cutout polygons can occur, which can become intricate

2) Interpolations: The projection of the ghost cell lies completely within one cell on the partner domain (see right side of Fig. 7). In this case a conservative interpolation from the coarse grid to the ghost cell is used. A two-dimensional Lagrange interpolation (Fig. 9) $\mathcal{L}^{\Omega_G}(X)$ delivers an interpolation of the state vector U and its derivatives from
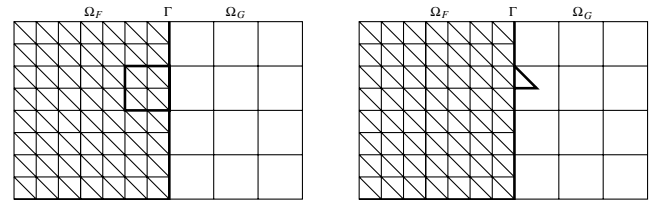

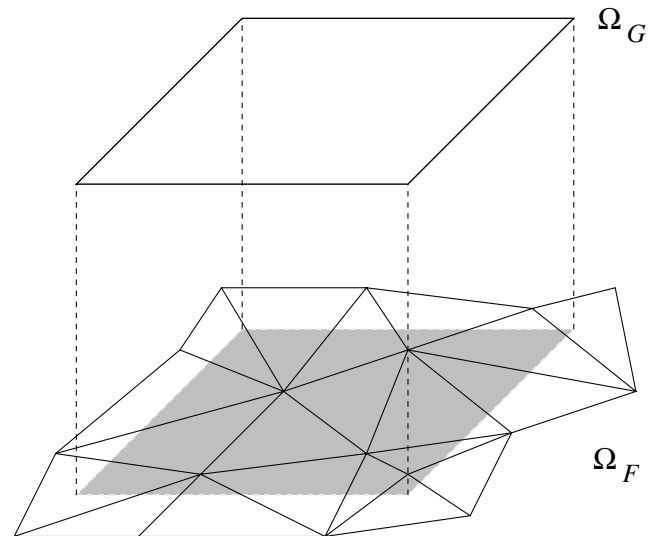**Fig. 7 Coupling different grids: averaging and interpolation.**

Fig. 8 Averaging by weighted volumes.

given integral mean values $\bar{U}^{\Omega_G}$ (the values that are stored in the cells). The integral mean values are obtained afterwards by a summation over the Gauss points with Gauss weights ω_i:

$$\bar{U}^{\Omega_F} = \sum_{i=1}^{N_{GP}} \omega_i U_{GP_i} \qquad (10)$$

$$U_{GP_i} = \mathcal{L}^{\Omega_G}(X_i) \qquad (11)$$

b. Gauss Point Coupling. The previously described coupling procedure was validated (see Sec. IV.B and Schwartzkopff [18]) and proved to be working very well with both structured and unstructured grids in two dimensions. However, determining the cutout polygons for the averaging case leads to complex algorithms. Furthermore, the treatment of "multidomain-ghost cells" (Fig. 12), ghost cells that overlap different neighboring domains, is very cumbersome. Those problems in 2-D can become painfully complex when the coupling procedure will be extended to 3-D. In the following, we propose a basic and unified coupling mechanism. The main idea is to treat both cases by interpolating the values from the neighbor grid onto the Gauss integration points of the ghost cell and then to integrate in order to obtain the integral mean values (Fig. 10). This allows a very generalized coupling procedure, as there is no difference between restrictions and interpolations anymore. The integration to get the integral mean value is independent of the way the interpolation onto the Gauss point was performed. The order of interpolation is set by the spatial order of the neighbor domain. Thus, the coupling domains can be of arbitrary size and discretization. For example, Fig. 10 shows a Cartesian ghost cell that belongs to a domain Ω_G with spatial accuracy $\mathcal{O}4$. The neighbor-domain is of spatial accuracy $\mathcal{O}5$ and
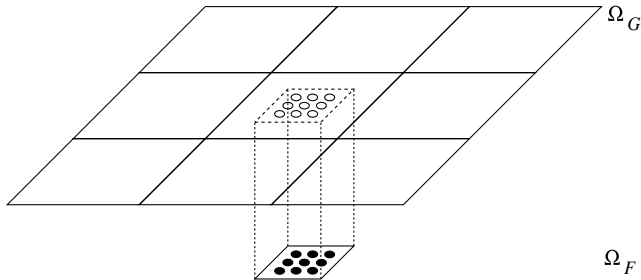

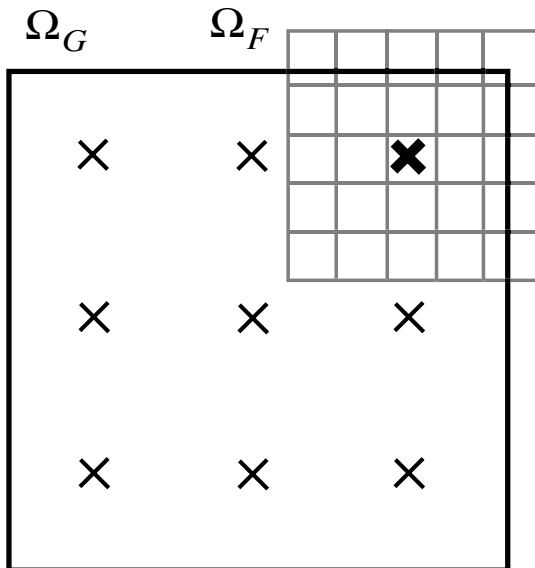**Fig. 9   Interpolation at the Gauss integration points.**

uses a corresponding 5×5 stencil for the 2-D Lagrange interpolation on the marked Gauss point. On the other hand, there even may be no stencil necessary: Fig. 11 shows a ghost cell coupling with an unstructured DG domain. As there is no reconstruction step for the very compact DG methods, all information can be obtained from the single neighbor-element in which the Gauss point lies. The unified coupling procedure also simplifies the treatment of multidomain cells (Figs. 12 and 13): The large cell in Fig. 13 from domain Ω_G depicts a cell that is similar to the gray colored ghost cell in Fig. 12 and overlaps two different domains Ω_{F1} and Ω_{F2}. The dashed line indicates the domain interface between the two neighbor domains Ω_{F1} and Ω_{F2}. Each Gauss point can be assigned a unique element of a neighboring grid that is the basis for the necessary interpolation stencil.

A distinction between restriction and prolongation has only to be made for the so-called Cauchy–Kovalevskaja (CK) procedure (see Sec. IV): if the ghost cell domain has a smaller time step than the neighbor domain, not only the state vector, but also its spatial
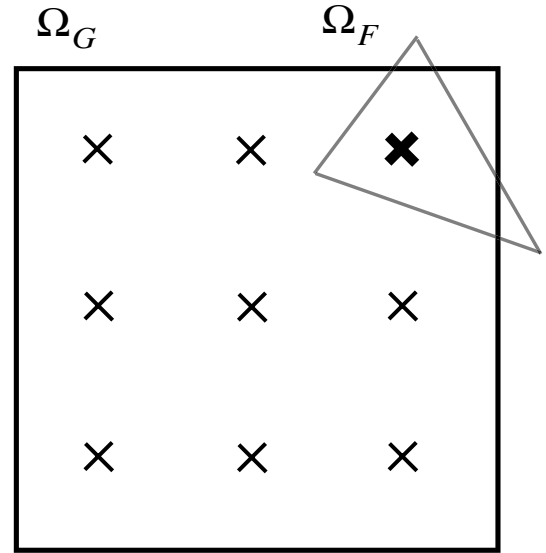

Fig. 11   Interpolation from a fine, unstructured (ADER-)DG grid Ω_F onto a Gauss point of the target ghost cell from domain Ω_G (spatial accuracy $\mathcal{O}4$).
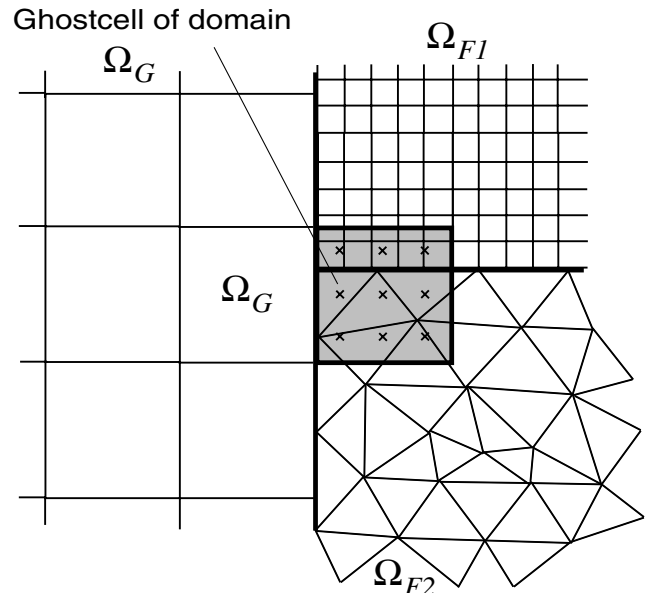

Fig. 10   Interpolation from a fine, structured (ADER-)FV grid Ω_F (spatial accuracy $\mathcal{O}5$) onto a Gauss point of the target ghost cell from domain Ω_G (spatial accuracy $\mathcal{O}4$).

Fig. 12   A multidomain cell: a ghost cell from domain Ω_G couples with both domains Ω_{F1} and Ω_{F2}.
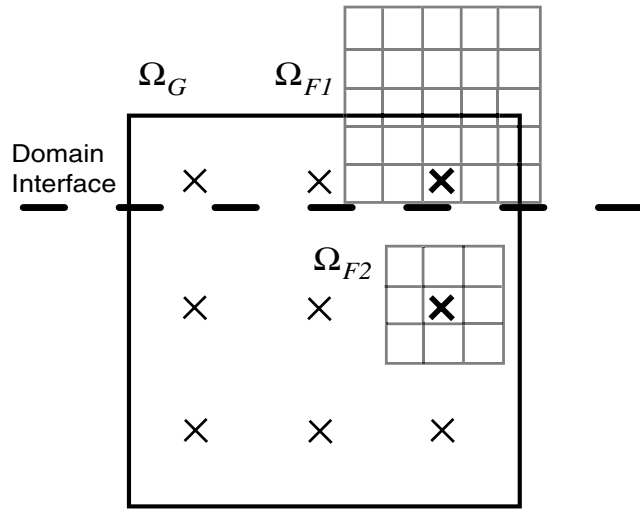
Fig. 13 Treatment of multidomain-cells using Gauss point coupling: The Gauss points from Ω_G's ghost cell obtain their values from different domains Ω_{F1} (spatial accuracy $\mathcal{O}5$) and Ω_{F2} (spatial accuracy $\mathcal{O}3$).

derivatives have to be determined at the Gauss point location. The coupling procedure may, however, not be fully conservative anymore regarding the integral mean values in the averaging case. Not every fine cell that lies within the coarse ghost cell's projection is considered anymore for the integral mean value. An investigation of the new coupling model's properties regarding conservation and reflections is the subject of current work. The following results refer to the fully conservative coupling method.

c. High-Frequency Perturbations. The conservative coupling procedure is examined for a problem that arises in the case when two coupling grids have different mesh sizes:

A wave with wavelength λ is represented by $\text{PPW} = \lambda/\Delta x$ (points per wavelength). For domain Ω_1, Δx_1 is chosen in a way that $\text{PPW}_1 > 3$ and a high-frequency wave can be resolved on the fine grid. For Ω_2, Δx_2 is chosen in a way that $\text{PPW}_2 < 3$. Hence, the wave cannot be resolved anymore on the coarse grid. Now it will be observed what happens when the wave crosses the interface Γ from Ω_1 to Ω_2.

As initial condition, a perturbation in the pressure is prescribed according to the *aliasing* problem by Tam [19]:

$$\begin{bmatrix} \rho' \\ u' \\ v' \\ p' \end{bmatrix} = \begin{bmatrix} 0 \\ 0 \\ 0 \\ [2 + \cos(\alpha x)]e^{-(\ln 2)(x/10)^2} \end{bmatrix} \quad (12)$$

with

$$\begin{bmatrix} \rho_0 \\ u_0 \\ v_0 \\ p_0 \end{bmatrix} = \begin{bmatrix} 1 \\ 0 \\ 0 \\ 1 \end{bmatrix} \quad (13)$$

$$\alpha = 1.7 \quad (14)$$

The constant values of the mean background flow are U_0. The pressure perturbation splits into two parts running to the left and to the right. The area $\Omega = [-300:200]$ was divided into two domains $\Omega_1 = [-300:0]$ and $\Omega_2 = [0:200]$. The initial condition's pressure peak is located in Ω_1 at $x = -75$. The grid sizes are $\Delta x_1 = 0.5$ and $\Delta x_2 = 2.0$ and the ratio between the time steps is also $\Delta t_2/\Delta t_1 = 4$. The 6th order ADER–FV method was used on Cartesian grids. Figure 14 shows the initial condition both on the fine and the coarse grid. It is obvious that the method on the coarse mesh cannot capture the high frequencies. Figure 15 depicts the right pressure wave exactly at the point of time when it crosses the interface $\Gamma = \Omega_1 \cap \Omega_2$ (top) and at a time, when the pulse is past the interface (bottom).
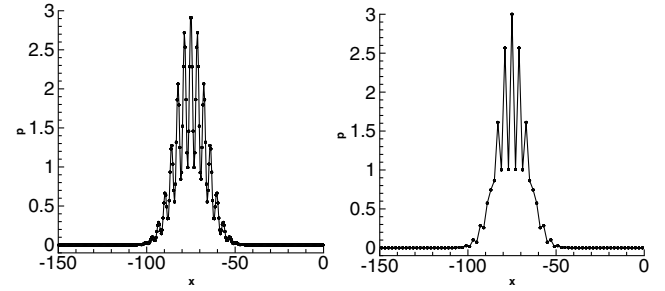

Fig. 14 Initial condition of the high-frequency perturbations. Fine grid on the left side, coarse grid on the right side.
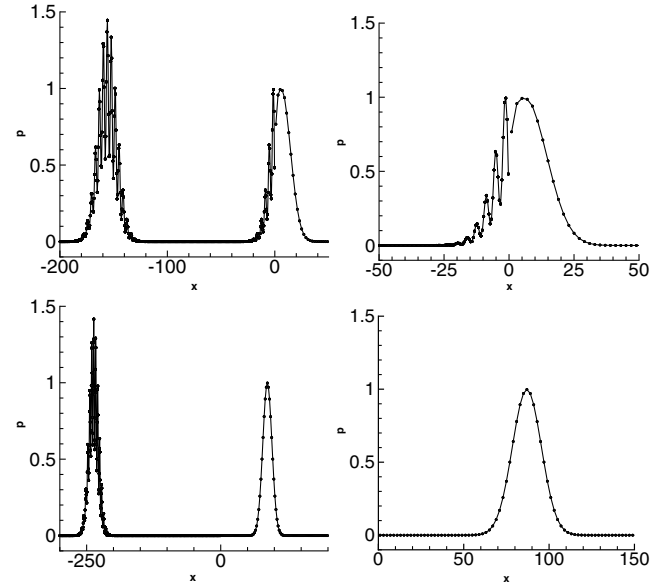

Fig. 15 Behavior regarding high-frequency perturbations. Top: State after $n = 150$ (crossing the interface); Bottom: After $n = 300$ (past the interface). Right sides: Zoom into the regions.
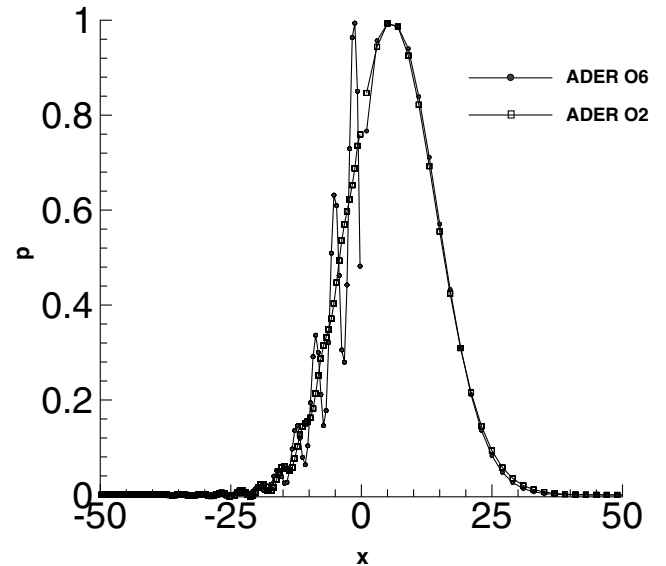

Fig. 16 Influence of the order of accuracy.

The wave cannot be captured anymore on Ω_2, but it leaves domain Ω_1 without interacting with the interface or triggering reflections.

In Fig. 16, the initial condition for different orders of accuracy shows that only high order methods are capable of resolving the high frequencies from the beginning. The 2nd order method dissipates almost all parts of the high frequencies, whereas the long wave
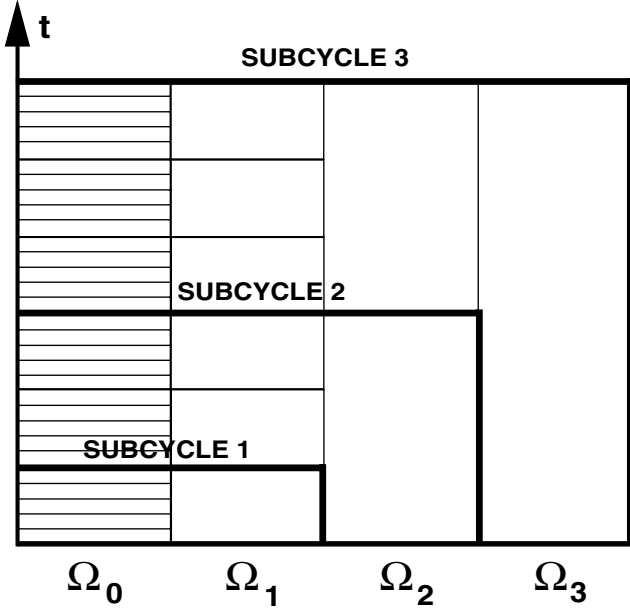
Fig. 17   Subcycles of a calculation with four differently sized domains.

Gaussian pulse is reproduced very well. A considerably finer mesh would have to be used here in order to achieve a similar quality of the initial solution which was obtained with the 6th order method. An analysis of both amplitude and phase error for different points per wavelength (PPW) for the ADER–FV scheme is given in Schwartzkopff [10].

3.   Coupling of Different Schemes

The coupling of different discretization methods causes no problems. Each method (DG and FV) uses the values in the ghost cells. We emphasize that there is a choice for the flux at the boundary Γ in domain Ω_1 to be different from the flux at the same boundary in Ω_2 as we do not define the flux but the data.

4.   Coupling of Different Time Steps

a.   Subcycles: Time Stepping and Data Exchange.   The idea of multisize meshes with different time steps has been examined by Tam et al. [20] for dispersion relation preserving (DRP) schemes on particularly designed grids. This basic idea has been extended in our approach for FV and DG schemes on arbitrary meshes.

The data between the domains are exchanged at the common time level. The local CFL number in each domain is adjusted such that neighboring domains have the same time level, if the domain with the larger time step is updated once. Meanwhile, the other domain has been updated n times with $n \geq 1$. The idea of subcycling is illustrated in Fig. 17: four domains Ω_0, Ω_1, Ω_2, and Ω_3 are coupled in a calculation. All four domains have different time steps ($\Delta t_{\Omega_0} < \Delta t_{\Omega_1} < \Delta t_{\Omega_2} < \Delta t_{\Omega_3}$) which have been adjusted in a way that each time step is a multiple of the previous one. For example, during only one time step of Ω_2, domain Ω_1 performs three steps. Depending on how many of the domains have reached the same absolute time level, subcycles 1, 2 or 3 are complete. For example after a subcycle of type 1, domain Ω_0 has made five time steps and shares now a common time level with Ω_1 and the domains can exchange data at their boundary $\Gamma_{\Omega_0,\Omega_1}$. When subcycle 3 is complete, all of the domains, Ω_0, Ω_1, Ω_2 and Ω_3, have arrived at the same time level. The updating procedure itself is sketched in Fig. 18 for the exchange between Ω_1 and Ω_2. The first step is the data exchange step, the second step and third steps are the data update steps in domain Ω_1, the fourth step is the data update in both domains Ω_1 and Ω_2. Then, the sequence would start again with step 1. The adaptation of the CFL number for each domain is done automatically at each subcycle.

The question is what to do with the ghost cells that are only updated every nth time step. In general, these are cells in a domain with a finer grid than the domain from which the values are taken. Thus these fine-grid ghost cells are interpolated from the coarse grid by a conservative interpolation. The key idea here is to use the Cauchy–Kovalevskaja (CK) procedure to update the ghost cells. The starting point is a Taylor series in time

$$U(X_0, t^n + \tau) = U(X_0, t^n) + \tau \frac{\partial U(X_0, t^n)}{\partial t} + \frac{\tau^2}{2} \frac{\partial U^2(X_0, t^n)}{\partial^2 t}$$

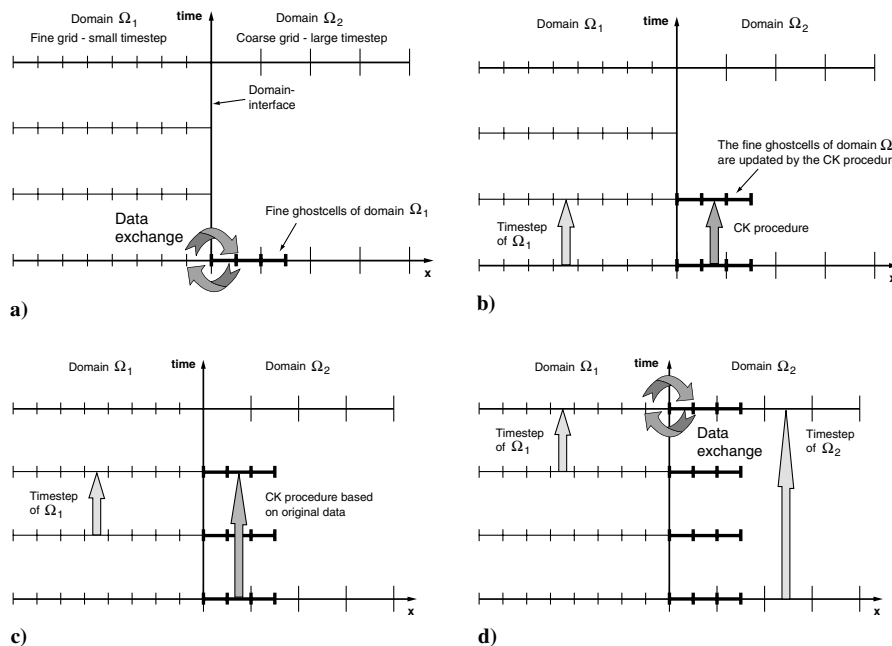$$+ \ldots + \frac{\tau^k}{k!} \frac{\partial U^k(X_0, t^n)}{\partial^k t} \tag{15}$$

Fig. 18   Coupling different time steps: a) Data exchange at the common time level: the states are interpolated onto the ghost cells of Ω_1 and Ω_2. For Ω_1, also the spatial derivatives are interpolated. b) time stepping of domain Ω_1. At the same time, its ghost cells are lifted to the new time level by the CK procedure. c) Ω_1 makes another time step. Again, its ghost cells are pushed to the new time level, based on the original data. d) Ω_2 performs one single time step and meets Ω_1 at a common time level again. Then, a new data exchange takes place.

The truncation order matches the chosen order of accuracy, for example, third order for a $\mathcal{O}3$ method in space and time. Time derivatives are now replaced by spatial derivatives with the Cauchy–Kovalevskaja procedure [21]. This procedure is used in Lax–Wendroff type time integration methods [21,22] and is also a main ingredient of the ADER scheme. The major advantage of this method is that once the derivatives at the point X_0 are known, the state at an arbitrary time $t^n + \tau$ can be calculated easily. Moreover, one does not have any dependency on a spatial scale from the fine-grid domain but only on the spatial scale from the interpolation on the coarse grid. As a consequence, these ghost cells inherit the stability condition from the coarse grid and every evaluation of the Taylor series between the two coarse grid time steps is in the stable range, although these ghost cells may have small sizes and the CFL number built with this small size is much larger than 1. If Ω_1 needs more than one intermediate time step then the update of the ghost cells is always based on the last common time level.

b. The Cauchy–Kovalevskaja Procedure for Linear Systems. In general, the CK procedure has to be applied to every Gauss point of the ghost cell that is supposed to be updated. However, for linear systems of equations, there exists a way to conveniently save memory and CPU time: in case every Gauss point of the ghost cell has the same interpolation stencil on the neighbor grid (which is often the case for prolongation elements), the cell can be integrated at an early stage at the time before the actual calculation when the coupling information is created. This is possible because the CK procedure for linear systems with constant coefficients does not depend on the values of the single Gauss points. Hence, there remains one Gauss point per ghost cell that has to be updated. For the procedure itself, an efficient implementation can be found. The CK procedure takes advantage of the original PDE in order to create time derivatives out of space derivatives: considering a set of 2-dimensional linear equations

$$U'_t + A U'_x + B U'_y = 0$$

it is possible to obtain the time derivatives just by reordering and differentiating:

$$U'_t = -A U'_x - B U'_y \tag{16}$$

$$U'_{tt} = -A U'_{xt} - B U'_{yt}, \qquad U'_{tx} = -A U'_{xx} - B U'_{yx},$$
$$U'_{ty} = -A U'_{xy} - B U'_{yy}, \tag{17}$$
$$U'_{tt} = A A U'_{xx} + A B U'_{yx} + B A U'_{xy} + B B U'_{yy}$$

In short, one can write

$$\frac{\partial^k U(X,t)}{\partial t^k} = (-1)^k \left(A \frac{1}{\partial x} + B \frac{1}{\partial y} \right)^k \partial^k U(X,t)$$

The following relation can be used:

$$\frac{\partial^{n+1,i,j} U}{\partial^{n+1} t \partial^i x \partial^j y} = -A \cdot \frac{\partial^{n,i+1,j} U}{\partial^n t \partial^{i+1} x \partial^j y} - B \cdot \frac{\partial^{n,i,j+1} U}{\partial^n t \partial^i x \partial^{j+1} y} \tag{18}$$

$$n \in [0, \ldots, \mathcal{O} - 2], \qquad i \in [0, \ldots, \mathcal{O} - 2 - n],$$
$$j \in [0, \ldots, \mathcal{O} - 2 - n - i]$$

To calculate the time derivative $\partial^{n+1}/\partial t^{n+1}$ for an arbitrary order, the time derivatives of level n, $\partial^n/\partial t^n$ with one higher space derivative are needed. The derivatives for $n = 0$ are known from the interpolation step itself. For example, the calculation of a 4th order time derivative would look like this:

n	i=0	i=1	i=2	i=3	i=4
0	0	x	xx	xxx	xxxx
1	0t	xt	xxt	xxxt	
2	0tt	xtt	xxtt		
3	0ttt	xttt			
4	0tttt				

c. The Cauchy–Kovalevskaja procedure for nonlinear systems. The nonlinear hyperbolic system of the two-dimensional Euler equations reads as

$$\begin{pmatrix} \rho \\ \rho u \\ \rho v \\ \rho E \end{pmatrix}_t + \begin{pmatrix} (\rho u) \\ (\rho u^2) + p \\ (\rho u v) \\ u(\rho E + p) \end{pmatrix}_x + \begin{pmatrix} (\rho v) \\ (\rho u v) \\ (\rho v^2) + p \\ v(\rho E + p) \end{pmatrix}_y = 0 \tag{19}$$

with the equation of state

$$p = (\gamma - 1)[\rho E - \tfrac{1}{2}(\rho u^2 + \rho v^2)] \tag{20}$$

In addition to the four conservative variables density (ρ), x momentum (ρu), y momentum (ρv), and total energy per mass unit (ρE), we use the auxiliary variables u, v, ρu^2, ρv^2, $\rho u v$ and the pressure p during the computation of the CK procedure.

As it is even more important in the nonlinear case than in the case of linear hyperbolic systems, an efficient algorithm to carry out the CK procedure has to be found. Although this seems to become cumbersome, there exists an efficient algorithm for the two-dimensional Euler equations, proposed by Dyson [23]. It may be generalized to three space dimensions in a straightforward manner. The method is based on the generalized Leibniz rule, which gives the space-time derivatives of arbitrary order for a product of multivariate scalar functions f and g:

$$\mathcal{L}^{(a,b,c)}(f,g) := \frac{\partial^{a+b+c}[f(x,y,t)g(x,y,t)]}{\partial x^a \partial y^b \partial t^c}$$

$$= \sum_{i=0}^{a} \sum_{j=0}^{b} \sum_{k=0}^{c}$$

$$\times \left[\binom{a}{i} \binom{b}{j} \binom{c}{k} \frac{\partial^{(a-i)+(b-j)+(c-k)} f}{\partial x^{(a-i)} \partial y^{(b-j)} \partial t^{(c-k)}} \cdot \frac{\partial^{i+j+k} g}{\partial x^i \partial y^j \partial t^k} \right] \tag{21}$$

This rule alone is not yet sufficient to treat the nonlinear Euler equations, because there appears for example a term like $(\rho u) u$ in the momentum flux, but u and its derivatives are not known a priori, but only those of the conservative variables ρ and ρu. The trick now consists in reformulating the Leibniz rule [Eq. (21)] to calculate all the space-time derivatives of the auxiliary variable u from the known space-time derivatives of ρ and ρu and all previously computed space-time derivatives of lower order of the auxiliary variable u. This is achieved by a modified Leibniz rule of the form

$$\mathcal{L}_{**}^{(a,b,c)}(fg,f,g) := \frac{\partial^{a+b+c}g(x,y,t)}{\partial x^a \partial y^b \partial t^c} = \frac{1}{f}$$
$$\cdot \left[\frac{\partial^{a+b+c}[f(x,y,t)g(x,y,t)]}{\partial x^a \partial y^b \partial t^c} \right.$$
$$\left. - \mathcal{L}_*^{(a,b,c)}(f,g) \right] \qquad (22)$$

with $f \neq 0$. The operator $\mathcal{L}_*^{(a,b,c)}(f,g)$ only contains lower order derivatives of g and is defined as the original Leibniz rule [Eq. (21)] except of the last term in the sum:

$$\mathcal{L}_*^{(a,b,c)}(f,g) = \underbrace{\sum_{i=0}^{a}\sum_{j=0}^{b}\sum_{k=0}^{c}}_{i+j+k \neq a+b+c}$$
$$\times \left[\binom{a}{i}\binom{b}{j}\binom{c}{k} \frac{\partial^{(a-i)+(b-j)+(c-k)}f}{\partial x^{(a-i)}\partial y^{(b-j)}\partial t^{(c-k)}} \cdot \frac{\partial^{i+j+k}g}{\partial x^i \partial y^j \partial t^k} \right],$$
$$\text{with } \mathcal{L}_*^{(0,0,0)}(f,g) := 0 \qquad (23)$$

B. Validation of the Coupling Procedure

The conservative coupling approach was validated in an extensive series of numerical experiments. The behavior toward high-frequency perturbations and changing equations has already been treated in Sec. IV.A. Two additional selected examples in which the linearized Euler equations (LEE) are solved shall be presented here. In both examples, a two-dimensional Gaussian pulse in density is transported through the calculation area with constant advection speed. To eliminate the influence of the numerical errors of the methods themselves, the 9th order ADER–FV scheme is used. Convergence studies were performed in order to show the high order accuracy of the whole system of coupled domains. The boundary conditions were also treated in 9th order. Therefore, the order of convergence should be of 9th order for the entire coupled calculation area in the ideal case.

1. Partitioning

First of all, the basic coupling mechanisms are examined. For this purpose, the calculation area is divided into 24 subdomains (Fig. 19), without changing anything regarding the grids, equations, or methods. Some of the depicted domains are too small to be plotted correctly by the visualization program (parallel lines in the upper picture of Fig. 19). The partitioning even includes domains that consist only of one single cell. The solutions of the calculations match exactly. Besides the startup time for creating the connectivity information between the single subdomains, the overall CPU time for the partitioned calculation (performed on a single processor computer) is higher than the CPU time for the reference calculation with one domain. The time that is necessary for the data exchange itself is about 5% of the overall time. The overhead is caused by the subroutine for the setting of the coupling ghost cells which has to be called more often as the number of additional ghost cells is strongly dependent on the number of partitions. In this extremely partitioned example, the overhead compared with the single domain solution is about 50%.

2. Changing Grids with Different Time Steps

The calculation area Ω is now divided in two domains Ω_1 and Ω_2. Again, the advection of the Gaussian pulse is examined: the pulse starts in Ω_1 and gets transported to Ω_2, where the calculation ends. The error norms are determined then. Domain Ω_2 has a larger cell size than Ω_1 ($\Delta x_{\Omega_1} < \Delta x_{\Omega_2}$) in the first two cases and vice versa in a third one. Both grids are refined in an equal ratio for determination of the order of convergence. For the time steps, the same ratio as for the grid sizes is chosen ($\Delta x_2/\Delta x_1 = \Delta t_2/\Delta t_1 = 2$ in the first, $\Delta x_2/\Delta x_1 = \Delta t_2/\Delta t_1 = 4$ in the second, and $\Delta x_2/\Delta x_1 = \Delta t_2/\Delta t_1 = \frac{1}{4}$ in the third case). First of all, the ghost cells of the finer domain with the smaller time step is not updated and integrated in time via the CK procedure. Therefore, they keep the value of the last data exchange. Table 2 shows the error norms and convergence rates: It is obvious, that only a 1st order convergence could be achieved, although both domains used 9th order methods. The experiment is repeated with the CK procedure switched on for the ghost cells. Table 3 now shows full 9th order of convergence in the error norms for the coupled calculation. Thus, it has been proved that a precise simulation in time in very high order is possible, even for changing grid sizes and time steps. This is one of the most important features of the coupling mechanism that leads to a tremendous decrease of CPU time without sacrificing accuracy.

V. Numerical Results

A. Coupling ADER–DG and ADER–FV: Numerical Convergence

In the following numerical examples, we show that the same behavior toward convergence as in the validation part of Sec. IV is obtained when ADER–DG domains are coupled to other ADER–DG domains or ADER–FV domains with different time steps.

The general computational setup is as follows: we solve the linearized Euler equations with the background flow $\rho_0 = 1$, $u_0 = 1$, $v_0 = 0$, and $p_0 = 1/\gamma$ in the two domains $\Omega_1 = [0; 50] \times [0; 50]$ and $\Omega_2 = [50; 100] \times [0; 50]$ using 4th order schemes in both domains. The initial condition at $t = 0$ with $\sigma = 5$ is

$$\rho'(0) = e^{-(1/2)[(x-25)^2+(y-25)^2]/\sigma^2}, \qquad u'(0) = v'(0) = p'(0) = 0 \qquad (24)$$

The exact reference solution of this problem at time $t = 50$ is given by

$$\rho'(50) = e^{-(1/2)[(x-75)^2+(y-25)^2]/\sigma^2},$$
$$u'(50) = v'(50) = p'(50) = 0 \qquad (25)$$

In our first computation, we use two ADER–DG domains with regular unstructured grids that do not conform at the boundary. In both grids we use the maximum possible time step, leading to a ratio
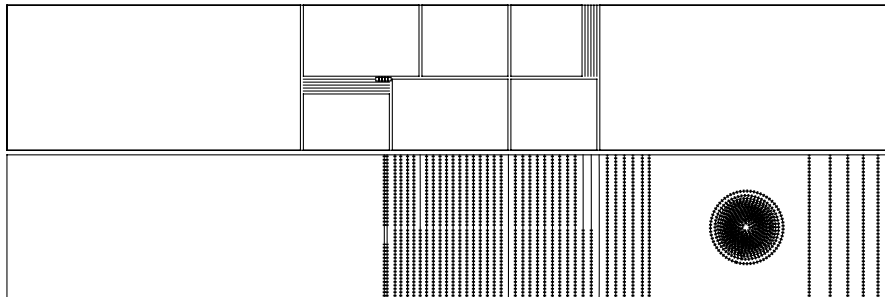

Fig. 19 Comparison of the solution on one grid with the solution on a calculation area that has been divided in 24 subdomains (the density is plotted). Top: Illustration of the single partitions. Bottom: Contour lines of the solution (dotted: solution from the partitioned solution; lines: solution from the unpartitioned reference domain).

Table 2 Error norms and orders of convergence in Ω_2 for the case of changing grids with different time steps $\Delta t_2/\Delta t_1 = \Delta x_2/\Delta x_1$. The ghost cells are not integrated in time with the CK procedure

#	$\Delta x_2/\Delta x_1$	Ω_2	L_∞ error	L_1 error	L_∞ order	L_1 order
1	2	150×50	$9.71074E-04$	$2.67910E-05$	–	–
2	2	225×75	$6.47382E-04$	$1.78773E-05$	1.0	1.0
3	2	300×100	$4.85993E-04$	$1.34097E-05$	1.0	1.0
4	2	375×125	$3.89048E-04$	$1.07284E-05$	1.0	1.0
1	4	80×26	$1.10042E-03$	$1.09415E-04$	–	–
2	4	120×39	$7.37393E-04$	$7.33741E-05$	1.0	1.0
3	4	160×52	$5.52716E-04$	$5.51462E-05$	1.0	1.0
4	4	200×65	$4.42873E-04$	$4.42760E-05$	1.0	1.0
1	1/4	280×104	$2.17131E-02$	$2.44640E-03$	–	–
2	1/4	420×156	$1.44238E-02$	$1.62613E-03$	1.0	1.0
3	1/4	560×208	$1.08050E-02$	$1.21809E-03$	1.0	1.0
4	1/4	700×260	$8.63941E-03$	$9.73842E-04$	1.0	1.0

Table 3 Error norms and orders of convergence in Ω_2 for the case of changing grids with different time steps $\Delta t_2/\Delta t_1 = \Delta x_2/\Delta x_1$. The ghost cells are integrated and updated in time with the CK procedure

#	$\Delta x_2/\Delta x_1$	Ω_2	L_∞ error	L_1 error	L_∞ order	L_1 order
1	2	150×50	$4.56111E-06$	$9.04538E-08$	——	——
2	2	225×75	$1.32447E-07$	$2.58487E-09$	8.7	8.8
3	2	300×100	$1.03001E-08$	$1.99641E-10$	8.9	8.9
4	2	375×125	$1.40747E-09$	$2.70982E-11$	8.9	8.9
1	4	80×26	$1.23498E-03$	$2.97428E-05$	——	——
2	4	120×39	$6.06183E-05$	$1.08607E-06$	7.4	8.2
3	4	160×52	$5.00610E-06$	$8.95367E-08$	8.7	8.7
4	4	200×65	$7.36905E-07$	$1.27843E-08$	8.6	8.7
1	$\frac{1}{4}$	280×104	$1.54786E-03$	$3.56406E-05$	——	——
2	$\frac{1}{4}$	420×156	$6.24332E-05$	$1.27408E-06$	7.9	8.2
3	$\frac{1}{4}$	560×208	$5.30053E-06$	$1.05903E-07$	8.6	8.6
4	$\frac{1}{4}$	700×260	$7.47070E-07$	$1.51503E-08$	8.8	8.7

Table 4 Convergence rates for coupling two ADER–DG $\mathcal{O}4$ domains *with* the CK procedure on the domain interface

N_G	L^∞	L^1	L^2	$\mathcal{O}_{L^\infty}$	$\mathcal{O}_{L^1}$	$\mathcal{O}_{L^2}$
10/19	$1.41554E-03$	$2.16305E-02$	$2.22552E-03$			
20/38	$9.12429E-05$	$1.47782E-03$	$1.60463E-04$	3.96	3.87	3.79
30/57	$3.45024E-05$	$3.00860E-04$	$3.45277E-05$	2.40	3.93	3.79
40/76	$1.07109E-05$	$9.62131E-05$	$1.10751E-05$	4.07	3.96	3.95

Table 5 Convergence rates for coupling of fastADER $\mathcal{O}4$ and ADER–DG $\mathcal{O}4$ domains *with* the CK procedure

N_G	L^∞	L^1	L^2	$\mathcal{O}_{L^\infty}$	$\mathcal{O}_{L^1}$	$\mathcal{O}_{L^2}$
20/10	$2.03021E-01$	$1.05524E+01$	$9.14841E-01$			
40/20	$3.81902E-02$	$1.78482E+00$	$1.58902E-01$	2.41	2.56	2.53
60/30	$9.51515E-03$	$4.04211E-01$	$3.49496E-02$	3.43	3.66	3.73
80/40	$3.65000E-03$	$1.45833E-01$	$1.15907E-02$	3.33	3.54	3.84

of the time steps of 1.9:1. It can be shown that, if the CK procedure is not applied, the global order of accuracy decreases to 1.5 on the finest grid. In the next computation we use the CK procedure to update the ghost cells and obtain the results shown in Table 4: the method proves to be globally 4th order accurate. We perform a third computation in which we couple a Cartesian ADER–FV domain Ω_1 with an ADER–DG domain Ω_2. Because of the more restrictive CFL condition in the fourth order ADER–DG domain, the time step ratio now is about 15:1. The calculation (again with the CK procedure) globally restores almost 4th order of accuracy (Table 5).

B. Single Airfoil Gust Response Problem

The single airfoil gust response by Scott [24] (problem 1 from category 3) has been calculated. The results presented here are for test cases 1 and 2, a Joukowski profile with 12% thickness ratio, a free stream Mach number of $Ma_\infty = 0.5$. In case 1, the profile has a camber ratio of zero and an angle of attack of $\alpha = 0$ deg, in case 2, the profile has a camber ratio of 0.02 and an angle of attack of

$\alpha = 2$ deg. In the inflow condition a vortical gust is prescribed with

$$\begin{bmatrix} u \\ v \end{bmatrix} = \begin{bmatrix} u_0 \\ 0 \end{bmatrix} + \epsilon \begin{bmatrix} -\sqrt{2}/2 \\ \sqrt{2}/2 \end{bmatrix} \cos[k(x+y) - kt] \quad (26)$$

$$\epsilon = 0.02 \quad (27)$$

$$k = \{0.1, 2.0\} \quad (28)$$

Case 1 is calculated at first with a low gust frequency ($k = 0.1$) and a high gust frequency ($k = 2.0$), then case 2 with $k = 2.0$ is calculated. Among the other parts of the benchmark problem, the first and the last part can be considered to be the easiest (due to the low frequency) and the most difficult (due to the high frequency) example to test the numerical methods and the domain decomposition. In our approach, there is no difference in complexity between calculating case 2 with or without camber ratio, but for the airfoil with camber ratio, a
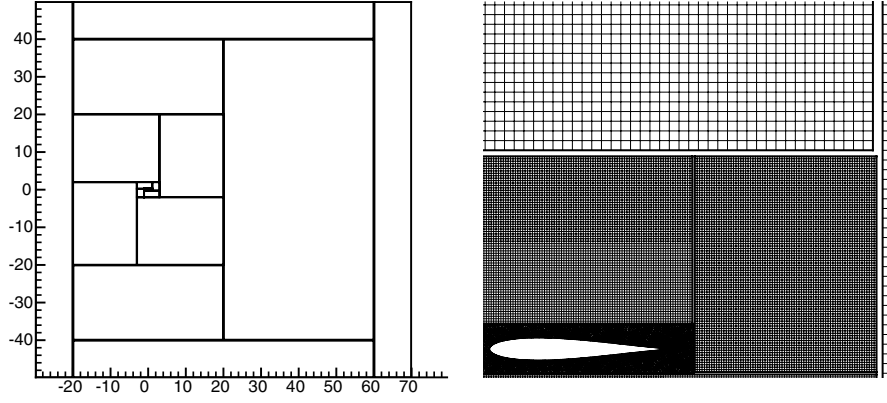
Fig. 20 Domains used for calculation. Left: Overview over all domains, including sponge layer domains. Right: Zoom of the core regions, where the nonlinear equations are solved.

numerical reference solution exists. The computational domain is $[-20.5, \ldots, 62] \times [-42, \ldots, 42]$. This domain is discretized with 1 unstructured domain and 11 structured domains, see Fig. 20 and Table 7. On the inner 5 domains the nonlinear Euler equations (EE) are solved and on the outer 7 domains we solve the linearized Euler (LEE) equations with 11th order of accuracy in space and time. As boundary conditions

$$t_{\text{factor}} = \frac{t_{\text{CPU}} \times N_{\text{processors}}}{A_{\text{domain}} \times t_{\text{end}} \times f_{\text{CPU}}} \qquad (29)$$

we use a further set of 4 structured domains where we apply a sponge layer [Eq. (32) in "V.E"]. Figure 21 shows the numerical solution (hydrodynamic + acoustic pressure, sponge layers not visible).

In case 1 with the low-frequency gust ($k = 0.1$), the solution is compared with the solution from a linear theory (Scott [24]). The solution for case 1 matches the reference solution very well and is shown in Fig. 22. For case 1 with $k = 2.0$ (Fig. 23), there are

unfortunately no reference data. Because of the varying gust frequencies, case 2 with $k = 2.0$ resembles case 1 with $k = 2.0$ more than case 1 with $k = 0.1$. For case 2 with $k = 2.0$, the linearized theory cannot be applied anymore for an accurate far-field solution because of the high frequency [25]. Here, the solution is compared with a numerical reference solution by Golubev [26], which is shown in Fig. 24. The solutions correlate also nicely, although the predicted amplitudes are a little bit too small.

Golubev et al. [26] also gives CPU times for his calculation: 47 hrs on a cluster of 16×2.4 GHz Linux machines. The calculation with the heterogeneous domain decomposition was performed on a Linux machine with a single 3.2 GHz processor. For comparison purposes, the CPU time per time and area unit is used. Also the number of processors and their clock frequency is considered (Table 6). Golubev's calculation area consists of two ellipses, which fit into a rectangle of the extents $[-10:10] \times [-15:15]$. All in all, Golubev calculates a smaller area in less wall-clock time, but with 16 processors. However, in terms of CPU time per calculated area, the heterogeneous coupling approach is faster (Table 6): If the larger domain decomposition area was calculated by Golubev's method with only one processor of the same specifications, the calculation would be 2 magnitudes of wall-clock time slower. Of course, this comparison is only a coarse approximation and does not necessarily allow the reverse if the calculation area is reduced to Golubev's domain for the domain decomposition approach. Large linear, and thus inexpensive areas would be left out, so that the ratio of CPU time per area would increase. On the other side, the comparison demonstrates the domain decomposition's potential of accelerating calculations in large domains. In this regard, Table 7 shows the percentage of total CPU time used by the single subdomains in

Table 6 Comparison of the calculations

	Golubev	Domain decomposition
t_{CPU}	47 h	115 h
$N_{\text{processors}}$	16	1
f_{CPU}	2.4	3.2
A_{domain}	<600	14,535
t_{end}	400	200
t_{factor}	$1.3E - 03$	$1.2E - 05$

Table 7 Percentage of the CPU time and of the total area of the calculation

|	CPU time [%]	Area fraction [%]	Discretization
Unstructured domain 01	14.4	0.01	ADER–DG, $\mathcal{O}3$, nonlinear EE
Structured domain 01	11.0	0.16	ADER–FV $\mathcal{O}4$, nonlinear EE
Structured domain 02	12.7	0.19	ADER–FV $\mathcal{O}4$, nonlinear EE
Structured domain 03	8.6	0.12	ADER–FV $\mathcal{O}4$, nonlinear EE
Structured domain 04	14.8	0.22	ADER–FV $\mathcal{O}4$, nonlinear EE
Structured domain 05	1.9	3.65	fastADER–FV $\mathcal{O}11$, LEE
Structured domain 06	1.9	3.65	fastADER–FV $\mathcal{O}11$, LEE
Structured domain 07	1.9	3.65	fastADER–FV $\mathcal{O}11$, LEE
Structured domain 08	1.9	3.65	fastADER–FV $\mathcal{O}11$, LEE
Structured domain 09	13.6	30.01	fastADER–FV $\mathcal{O}11$, LEE
Structured domain 10	1.9	7.64	fastADER–FV $\mathcal{O}11$, LEE
Structured domain 11	1.9	7.64	fastADER–FV $\mathcal{O}11$, LEE
Structured domain 12	0.2	18.57	fastADER–FV $\mathcal{O}5$, LEE
Structured domain 13	0.1	6.44	fastADER–FV $\mathcal{O}5$, LEE
Structured domain 14	1.9	7.96	fastADER–FV $\mathcal{O}11$, LEE
Structured domain 15	0.1	6.44	fastADER–FV $\mathcal{O}5$, LEE
Coupling procedure	11.0		Interpolation order $\mathcal{O}5$
Total	100.0	100.0	
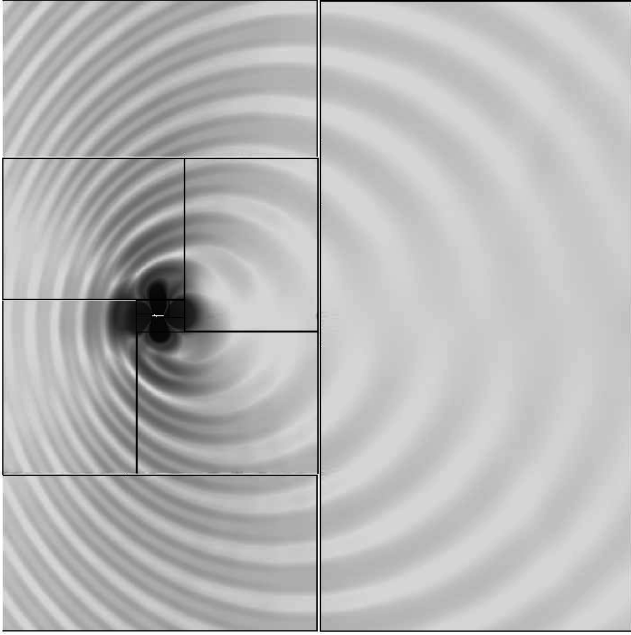
Fig. 21 Full acoustic + hydrodynamic solution $p = p_0 + p'$ for $k = 2.0$.

Fig. 23 Directivity pattern of the acoustic pressure for case 1 with $k = 2.0$.

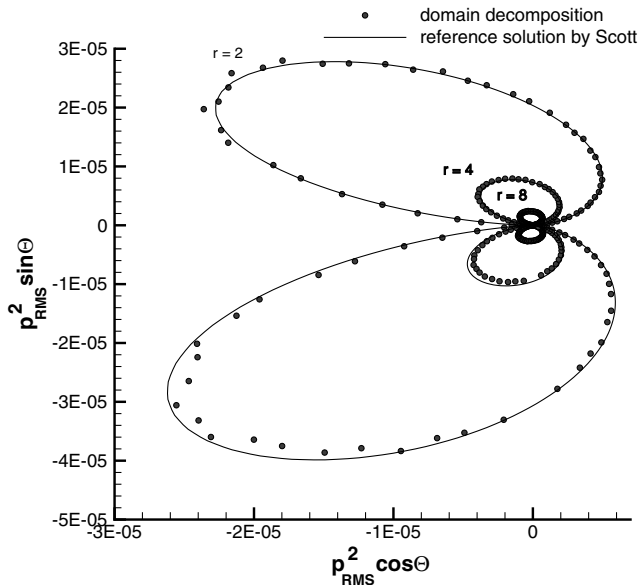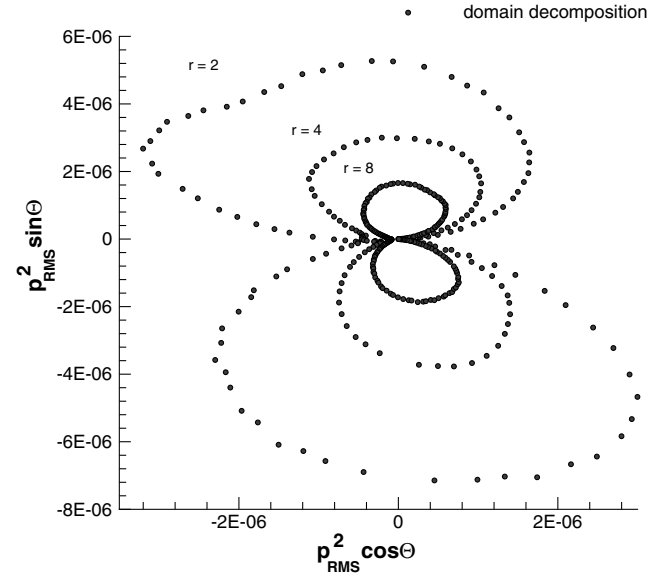
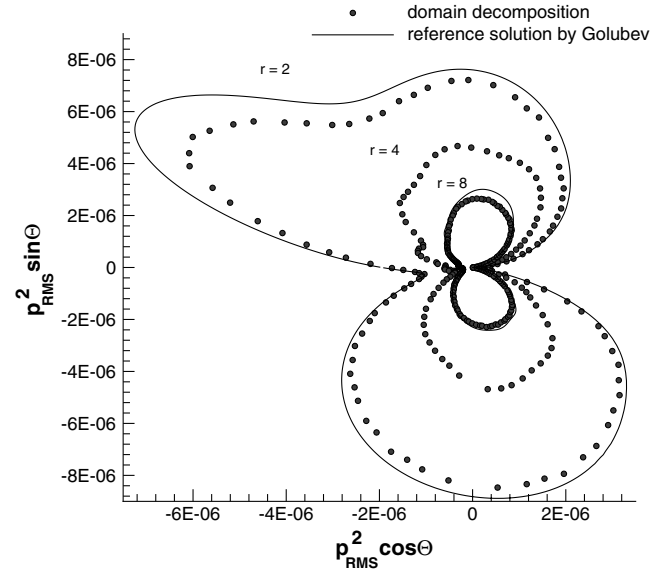Fig. 22 Directivity pattern of the acoustic pressure for case 1 with $k = 0.1$ together with the reference solution by Scott et al.

Fig. 24 Directivity pattern of the acoustic pressure for case 2 with $k = 2.0$ together with a reference solution by Golubev et al.

comparison with their area contribution for the coupled calculation. It is clear that the smallest areas with the high order nonlinear methods consume most of the CPU time, whereas the wave transport into the far-field is very inexpensive.

C. Transonic Flow

In addition to the previous single airfoil gust response in a subsonic regime at $Ma_\infty = 0.5$, the free stream Mach number has been raised now to $Ma_\infty = 0.9$ for case 2 with $k = 2.0$. At this flow speed, the airfoil becomes transonic and one can expect shocks. Indeed, two shocks are clearly visible on the suction and pressure side which cross the domain coupling interface without any effort (Fig. 25). Yet, the numerical schemes remain stable: an ENO-limiter by Harten, Engquist, Osher, and Chakravarthy [27] was applied to the reconstruction process for the nonlinear Cartesian ADER–FV domains.

D. Interface Transmission

The interface transmission problem by Tam [28] (problem 2 from category 1) has been calculated. An incident acoustic wave impinges on an interface between two fluids (Fig. 26). The two fluid domains possess the same mean background pressure $p_{0,1} = p_{0,2}$ but the sound speeds are different due to a jump in density. Part of the wave is now transmitted and refracted, part of it is reflected.

The governing equations for both domains are the linearized Euler equations with the parameters shown in Table 8. The dynamic and kinematic boundary conditions at the fluid interface are $p'_1 = p'_2$ and $v'_1 = v'_2$. The plane acoustic wave has the properties

$$\begin{pmatrix} \rho'_1 \\ u'_1 \\ v'_1 \\ p'_1 \end{pmatrix}_{\text{incident}} = \begin{pmatrix} 1.0 \\ -\sin\Theta \\ -\cos\Theta \\ 1.0 \end{pmatrix}$$
$$\cdot \cos[-\omega \cdot (\sin\Theta \cdot x + \cos\Theta \cdot y + t)] \qquad (30)$$

and is prescribed on the upper boundary of the domain of fluid 1. The frequency is $\omega = 0.7$ and the angle is $\Theta = 20$ deg in case 1 and $\Theta = 65$ deg in case 2, which means total reflection of the wave in the latter case.

In both cases, we use periodic boundaries on the left and on the right side. The domain of the calculation consists of 4 subdomains, 2 for each fluid. This is only due to implementation details of our code in order to be able to use periodic boundaries. Nevertheless, this additional partitioning has neither any effect on the quality of the calculation, nor significantly on the CPU time as it has been proved before in the validation section. To avoid reflections at the in- and outflow, a sponge layer [Eq. (32) in V.E] has been applied again at the upper and lower boundary which smoothly transforms the numerical solution from the interior of the domain into the exact inflow value on the edge. As there are no special requirements, a uniform mesh size has been chosen that is a multiple of the wavelength λ_x in x direction to ensure a periodic behavior. The extents are $5\lambda_x \times 5\lambda_x$ in the first case, $5\lambda_x \times 10\lambda_x$ in the second case, with $\lambda_x = 2\pi/(\omega \cdot \sin\Theta)$. The
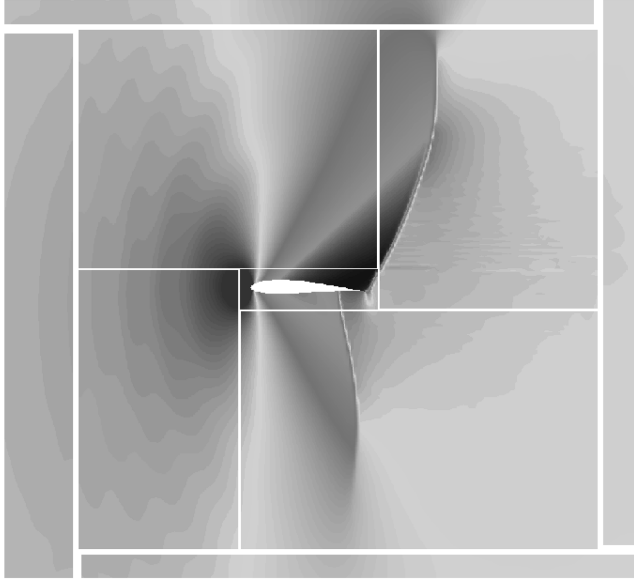
Fig. 25 Pressure contours for the full acoustic + hydrodynamic solution $p = p_0 + p'$ for a transonic flow at $Ma_\infty = 0.9$. Zoom into region.
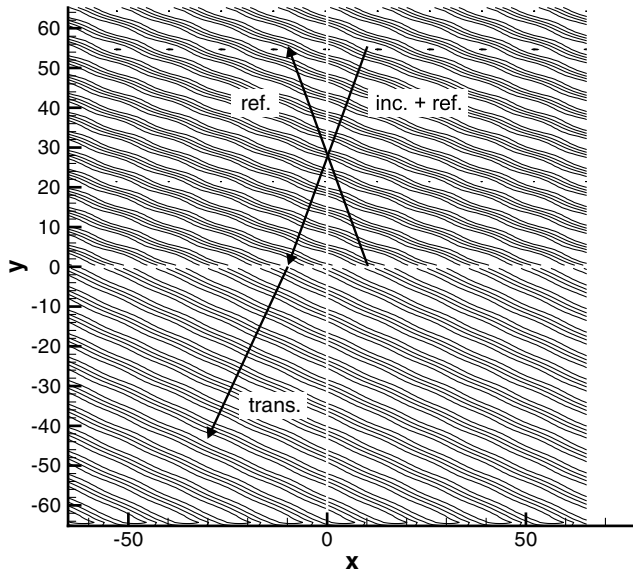
Fig. 26 FastADER $\mathcal{O}6$: contour levels for p' from −2 to 2 with increments of 0.4444; upper half plane: incident plus reflected waves; lower half plane: transmitted wave.

Table 8 Parameters of the domains. γ can be chosen arbitrarily

Fluid 1	Fluid 2
$u_{0,1} = 0.0$	$u_{0,2} = 0.0$
$v_{0,1} = 0.0$	$v_{0,2} = 0.0$
$\rho_{0,1} = 1.0$	$\rho_{0,2} = \alpha \cdot \rho_{0,1} = 0.694$
$p_{0,1} = 1/\gamma$	$p_{0,2} = 1/\gamma$

cell sizes were chosen as $\Delta x = \Delta y = \lambda x/30$. As the wavelength $\lambda = 2\pi/|k| = 2\pi/\omega = 8.976$ remains constant for both angles $\Theta = 20$ deg and $\Theta = 65$ deg, λ_x varies from $\lambda_x = 26.244$ (20 deg) to $\lambda_x = 9.904$ (65 deg). Thus, the points per wavelength are $PPW_{20\ deg} = 10.2$ and $PPW_{65\ deg} = 27.2$. A mesh refinement does not change the solution significantly, also a calculation with a coarser cell size of $\Delta x = \Delta y = \lambda x/18$ did not show differences, although the PPW become quite small.

1. Angle of Incidence $\Theta = 20$ deg

Figures 26 and 27 show the contour plot of the acoustic pressure and the cut sections along which the solution is compared with the analytical solution in Figs. 28–33 [numerical (solid) and analytical (dashed) solution for an angle of incidence of 20 deg with grid size $\Delta x = \Delta y = \lambda_x/30$; figures on left: fastADER $\mathcal{O}6$, figures on right: fastADER $\mathcal{O}9$]. The x-axis labels s_i, s_t, and s_r refer to the distances along the cut sections of the incident, the transmitted and the reflected wave. The numerical solutions for the incident and transmitted waves are in good accordance with the exact solution (Figs. 28–31). With low order schemes ($\mathcal{O}2$, $\mathcal{O}3$), an accurate capturing of the reflected waves proved difficult, which has to be investigated yet. For high order methods (such as $\mathcal{O}6$), the amplitude seems to be a little overestimated (Figs. 32 and 33). The question arises, how the nonconservative flux coupling affects the conservation of energy in case of the reflection at the "real" material interface. A more detailed analysis and a comparison with a conservative treatment is the subject to our current work. Also going to even higher order ($\mathcal{O}9$) does not decrease the amplitude of the reflection. The implementation of the nonreflecting boundary conditions also contributes to this behavior. Tests with an extended calculation area showed an improvement of the results.

2. Angle of Incidence $\Theta = 65$ deg: Total Reflection

For the total reflection case, the problem regarding the amplitude of the reflection does not seem to be present to that extent. However, the area where the data for the comparison was sampled is now
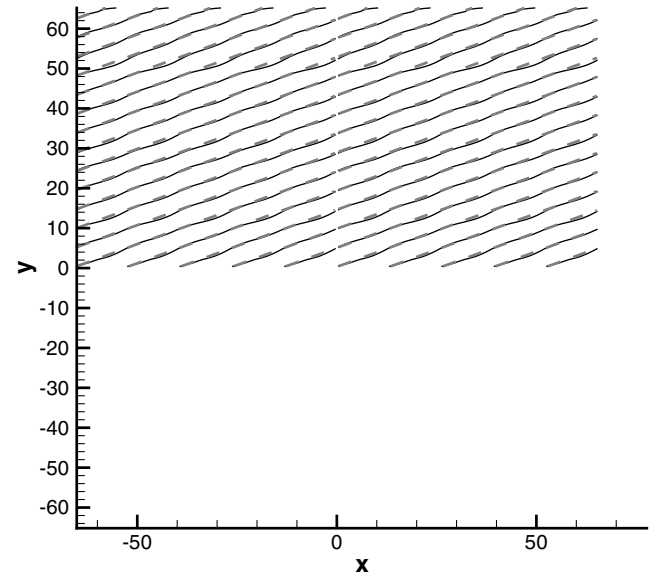

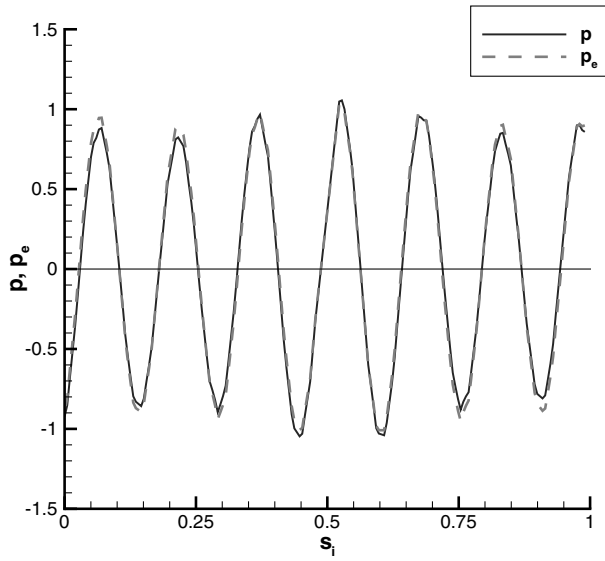**Fig. 27 FastADER $\mathcal{O}6$: zero pressure contours; reflected waves only.**

Fig. 28   FastADER $\mathcal{O}6$: incident plus reflected waves of the upper half plane.
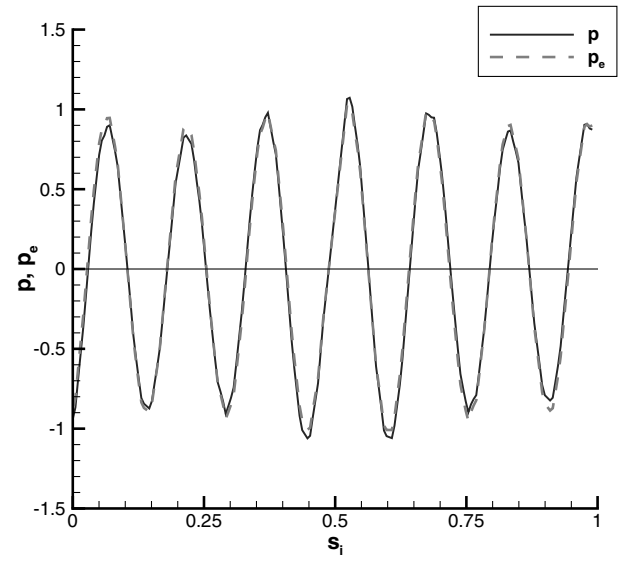

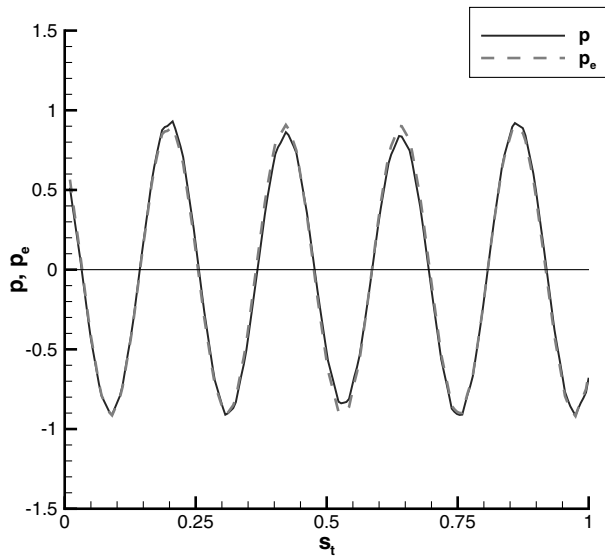Fig. 29   FastADER $\mathcal{O}9$: incident plus reflected waves of the upper half plane.

Fig. 30   FastADER $\mathcal{O}6$: transmitted waves of the lower half plane.
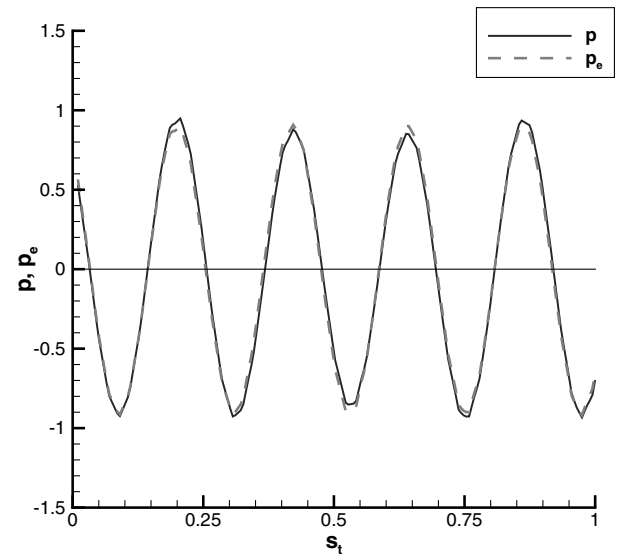

Fig. 31   FastADER $\mathcal{O}9$: transmitted waves of the lower half plane.
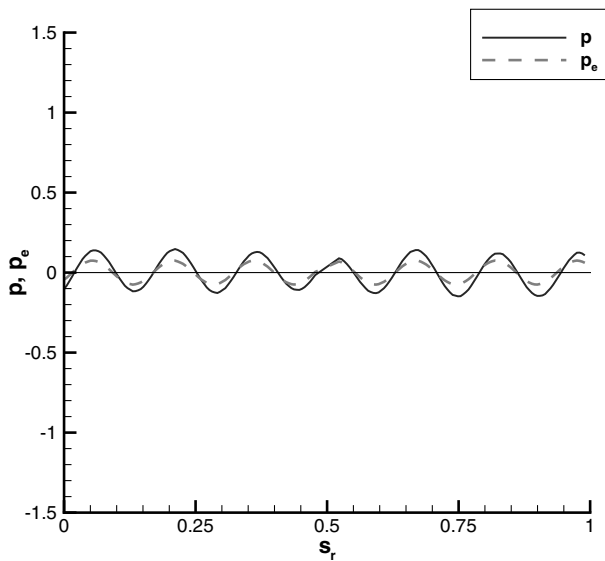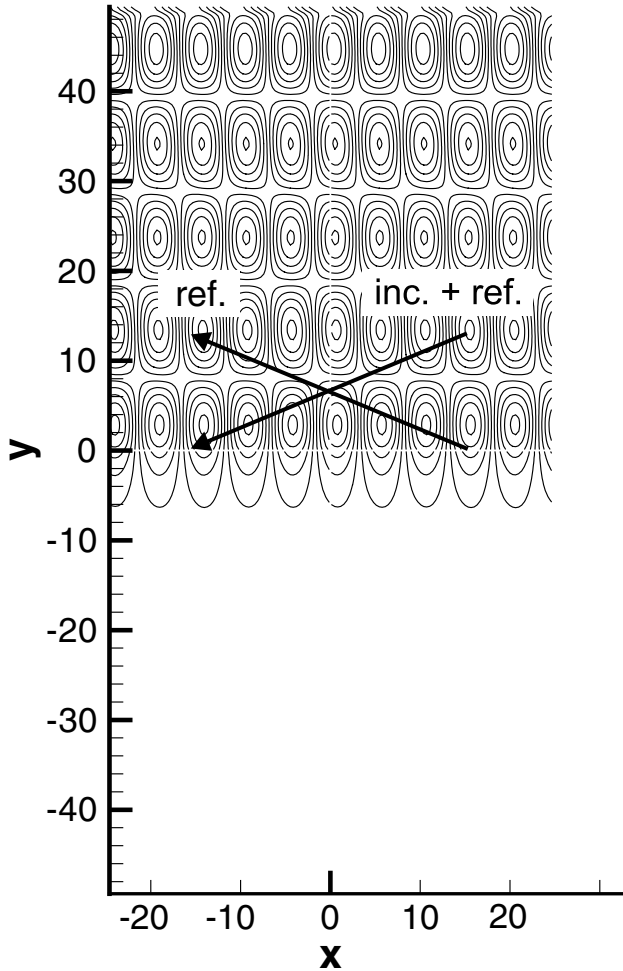

Fig. 32   FastADER $\mathcal{O}6$: reflected waves of the upper half plane.
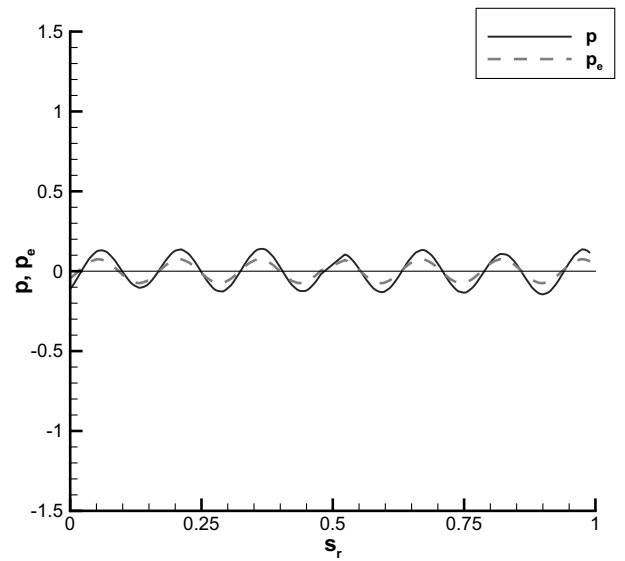
Fig. 33   FastADER $\mathcal{O}9$: reflected waves of the upper half plane.

Fig. 34 FastADER $\mathcal{O}6$: contour levels for p' from -2 to 2 with increments of 0.4444; upper half plane: Incident plus reflected waves; lower half plane: Transmitted wave.

Fig. 35 FastADER $\mathcal{O}6$: zero pressure contours; reflected waves only; numerical (solid) and analytical (dashed) solution.

located closer to the coupling interface, due to the angle of incidence. A decrease in the quality of the solution toward the upper inflow boundary can be observed in the contour plots Figs. 34 and 35 which again gives an indication that the implementation of the sponge layer might need some improvement. On the other hand, the solution is already quite good for the $\mathcal{O}3$ method and captures the total reflection property nicely (Figs. 36–39) [numerical (solid) and analytical (dashed) solution for an angle of incidence of 65 deg (total reflection) with grid size $\Delta x = \Delta y = \lambda_x$]. Again, the x-axis labels s_i and s_r refer to the distances along the cut sections of the incident and the reflected wave.

E. Acoustic Scattering of a Circular Cylinder

To validate the coupling between ADER–DG schemes on unstructured grids and ADER–FV schemes on Cartesian grids, we choose a nontrivial example for which, however, an analytical solution exists. We compute the scattering of a time harmonic plane sinusoidal acoustic pressure fluctuation incident on a single circular cylinder of radius R with perfectly reflecting walls. The plane wave travels in x direction and has the form

$$p'_{\text{in}}(\boldsymbol{x}, t) = e^{-I\omega t} e^{Ikx} = e^{-I\omega t} e^{Ikr\cos\theta} \qquad (31)$$

with the wave number k, the angular frequency ω and $I = \sqrt{-1}$.

For a derivation of the analytical solution see, for example, Morse and Feshbach [29]. For the numerical simulation, we solve the problem in a computational domain with extent $[-20; 20] \times [-20; 20]$ using the linearized Euler equations in all domains. The background flow, about which the Euler equations are linearized, is
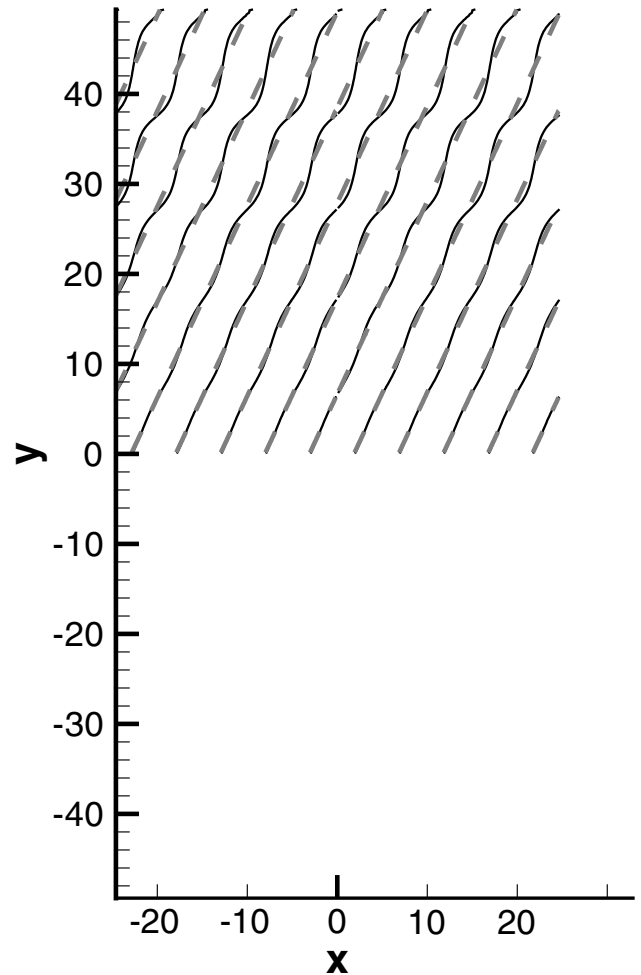
chosen as $\rho_0 = 1$, $u_0 = v_0 = 0$, and $p_0 = 1/\gamma$ leading especially to a speed of sound $c_0 = 1$. We use one unstructured domain of extent $[-2; 2] \times [-2; 2]$ containing the cylinder of radius $R = 1$ and four Cartesian blocks for discretizing the rest of the computational domain. On the unstructured mesh we use a 4th order ADER–DG
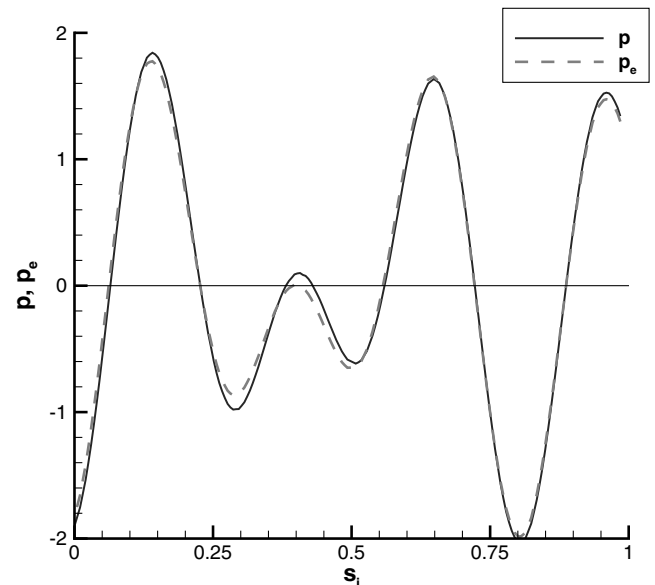

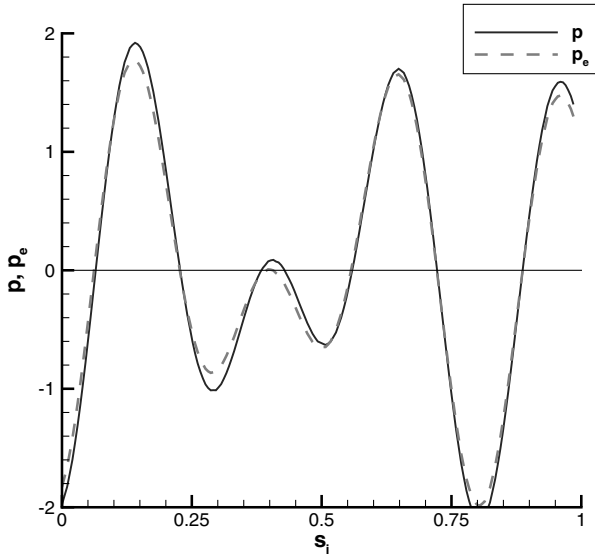Fig. 36 FastADER $\mathcal{O}3$: incident plus reflected waves of the upper half plane.

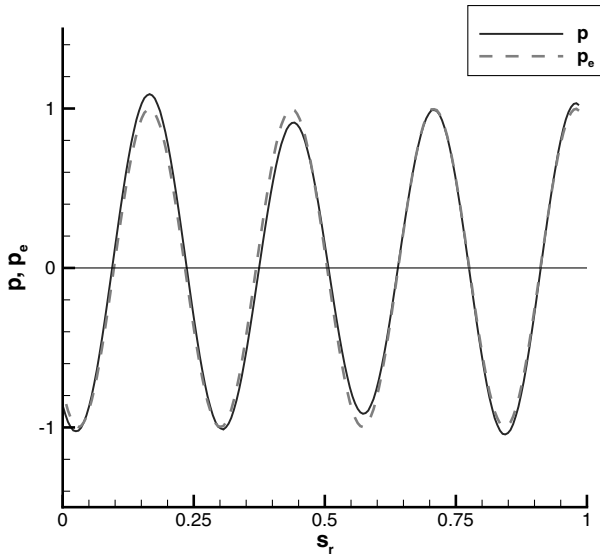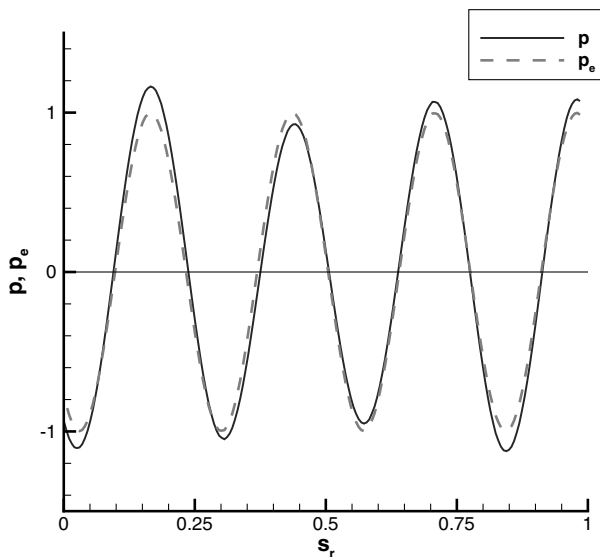**Fig. 37   FastADER $\mathcal{O}6$: incident plus reflected waves of the upper half plane.**

scheme and on the Cartesian grids we apply a sixth order fastADER scheme [10,11]. The initial condition is imposed such that it contains only fluctuations in the right-moving characteristic wave with an amplitude of the characteristic fluctuations of 1e-03. The cylinder wall is perfectly reflecting and the radiation boundary condition is imposed by a sponge layer. Because outgoing waves should leave without reflections and at the same time we must allow the incoming plane wave to enter the domain, we use a special sponge layer of the following form:

$$\tilde{u}_{ij}^{n+1} = (1-\sigma)u_{ij}^{n+1} + \sigma u_{\text{in}}(x_i, y_j, t^{n+1}) \qquad (32)$$

where u_{ij}^{n+1} is the time update of the numerical solution as computed by the numerical scheme, $\tilde{u}_{ij}^{n+1}$ is the modified numerical solution after applying the sponge layer, u_{in} is the entering plane wave, and $0 \leq \sigma \leq 1$ is the sponge parameter defined as
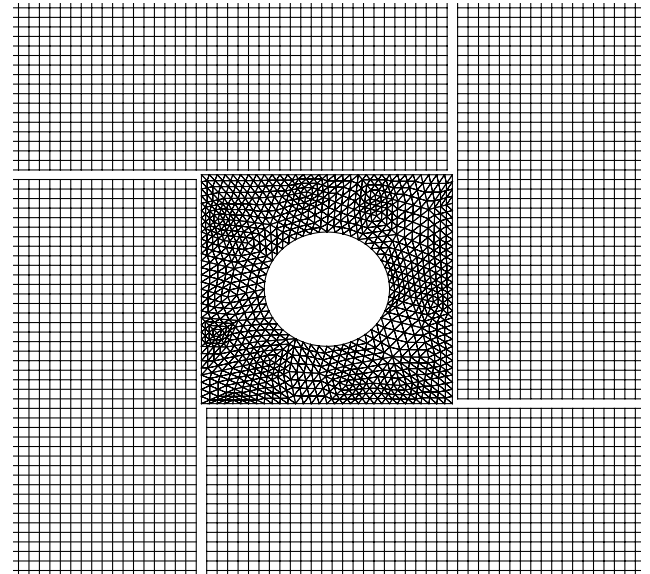

Fig. 38   FastADER $\mathcal{O}3$: reflected waves of the upper half plane.

Fig. 40   Domain decomposition for the cylinder scattering problem: zoom into the fine grid.

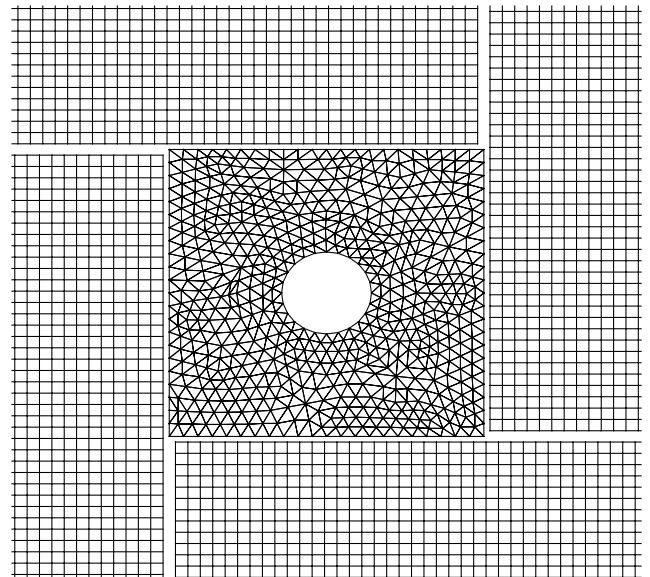**Fig. 39   FastADER $\mathcal{O}6$: reflected waves of the upper half plane.**

Fig. 41   Domain decomposition for the cylinder scattering problem: zoom into the coarse grid.

$$\sigma = \begin{cases} \left(\frac{L-\delta}{L} \right)^s & \text{if } \delta \leq L \\ 0 & \text{if } \delta > L \end{cases} \quad (33)$$

In (33), L denotes the thickness of the sponge layer, δ is the distance of the barycenter of cell Q_{ij} to the nearest boundary of the computational domain and s is the power of the sponge layer. In the following computations, we choose $L = 2$ and $s = 4$. Please note that if the sponge layer is applied to the cell averages according to (32), the scheme is only first order accurate at the boundaries.

We do several computations of this example, first with $k = 2$ on a fine grid with 2048 triangles in the unstructured mesh and 132×108 cells in each Cartesian block, corresponding to a resolution of about 20 points per wavelength. Figure 40 shows a zoom into the inner region ($[-5; 5] \times [-5; 5]$) of the fine-grid domain decomposition. For the unstructured domain the primal mesh is shown, for the Cartesian grids the dual mesh is plotted, explaining the gaps between the grids. A global view of the instantaneous field of the acoustic pressure
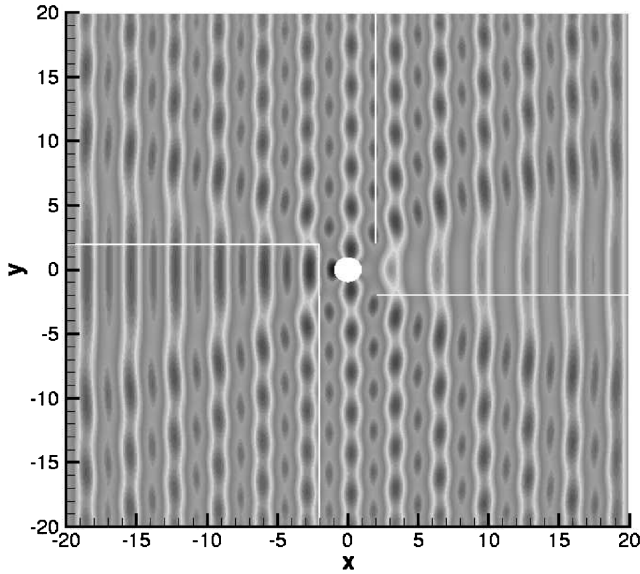
fluctuations in the entire domain is shown in Fig. 42 (Fig. 43 depicts the pressure fluctuation for $k = 4$). A very important piece of information for acousticians is the so-called directivity pattern, which shows the sound pressure level in a polar plot as a function of angle θ and distance r between observer and the center of the scatterer. Such a directivity pattern, obtained by our simulation, is shown in Fig. 44. The analytical solution is also shown in the same figure. Already in this geometrically simple case the directivity pattern has a quite complicated structure due to constructive and destructive interference between incident and scattered wave, depending on angle and distance. We note an excellent agreement of our simulation with the exact analytical reference solution.

Next, we solve the same problem ($k = 2$) on a two-times coarser grid in each space dimension, reducing the number of triangles in a slightly enlarged unstructured domain (new extent: $[-3.5; 3.5] \times [-3.5; 3.5]$) to 1152 and the number of cells in each Cartesian block to 85×60. The resolution is now about 11 PPW. Figure 41 shows again a zoom into the inner region ($[-7; 7] \times [-7; 7]$) of the computational domain. We note that the sound pressure level is still

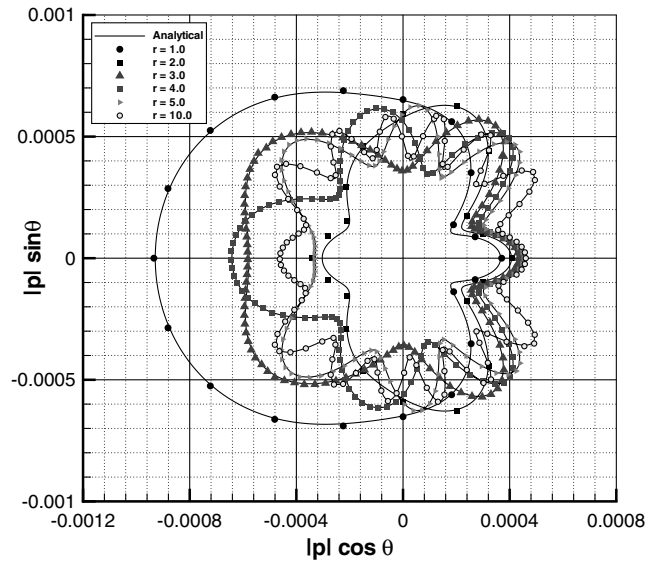**Fig. 42 Instantaneous field of the acoustic pressure fluctuation for $k = 2$ at $t = 100.0$.**

Fig. 44 Directivity patterns for the cylinder scattering problem with $k = 2$ obtained on the fine grid and comparison with the analytical solution.

Fig. 43 Instantaneous field of the acoustic pressure fluctuation for $k = 4$ at $t = 100.0$.
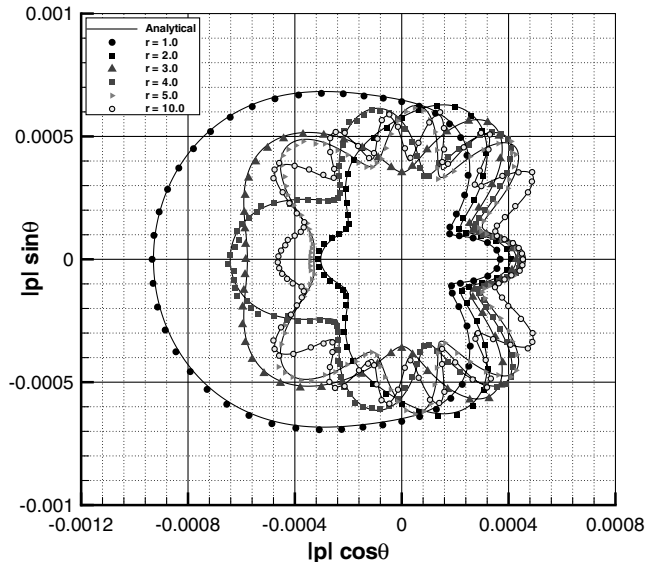

Fig. 45 Directivity patterns for the cylinder scattering problem with $k = 2$ obtained on the coarse grid and comparison with the analytical solution.
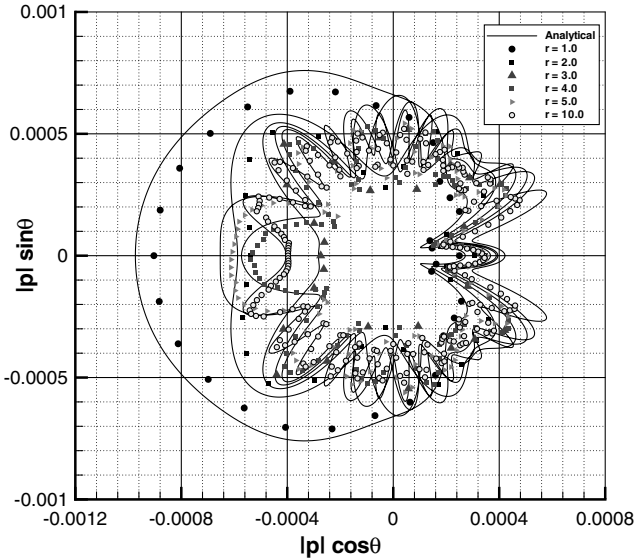
Fig. 46   Directivity patterns for the cylinder scattering problem with $k = 4$ **obtained on the coarse grid using a 6th order fastADER scheme and comparison with the analytical solution.**
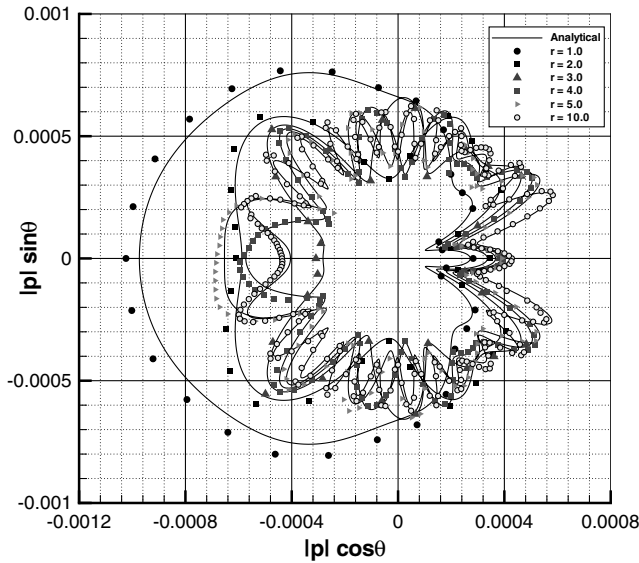

Fig. 47   Directivity patterns for the cylinder scattering problem with $k = 4$ **obtained on the coarse grid using a 12th order fastADER scheme and comparison with the analytical solution.**

very well predicted compared with the analytical solution, see Fig. 45.

Finally, we decrease the resolution to 5.5 PPW when solving the scattering problem for a wave number of $k = 4$ on the same grid as in the previous computation. The directivity pattern is compared with the analytical solution in Fig. 46 and we note that the numerical simulation globally predicts a too low sound pressure level because for the 6th order ADER–FV scheme that we used, the amplitude errors become significant in this PPW range [10,11]. If we increase the order of accuracy of the ADER–FV scheme to 12, we get the directivity patterns depicted in Fig. 47, showing a considerable improvement concerning the magnitude of the sound pressure level (SPL). Unfortunately, however, the SPL now is slightly overpredicted in some regions in front of the cylinder. This is most probably due to the sponge layer that reduces the boundary conditions to first order of accuracy. A slight asymmetry in the directivity patterns can be observed on the coarse grid (Figs. 45, 44, and 43), although the problem is symmetric, originally. This effect is due to the asymmetrical character of the unstructured grid around the cylinder.

On the fine grid, the solution is very good due to the high resolution (Fig. 40). On the coarse grid, the resolution decreases and slight asymmetries become visible. They are small for $k = 2$ and increase for the more difficult case $k = 4$. We emphasize that the 12th order ADER–FV scheme uses the same CPU time as a 4th order DRP scheme with 4th order Runge–Kutta timestepping, see Schwartzkopff [30].

F.   Multiple Acoustic Scattering

In the previous section, we validated the domain decomposition approach on a geometrically relatively simple scattering problem for which an analytical reference solution exists. In this section, we apply the approach to a more complicated multibody scattering problem. Here, the application of a triangular grid for discretizing the inner zone containing the scatterers is very convenient because the unstructured mesh can be generated in a completely automatic manner. For the discretization of the far field, four Cartesian blocks are used.

The configuration is as follows: we solve again the linearized Euler equations with the same mean flow as in the cylinder scattering
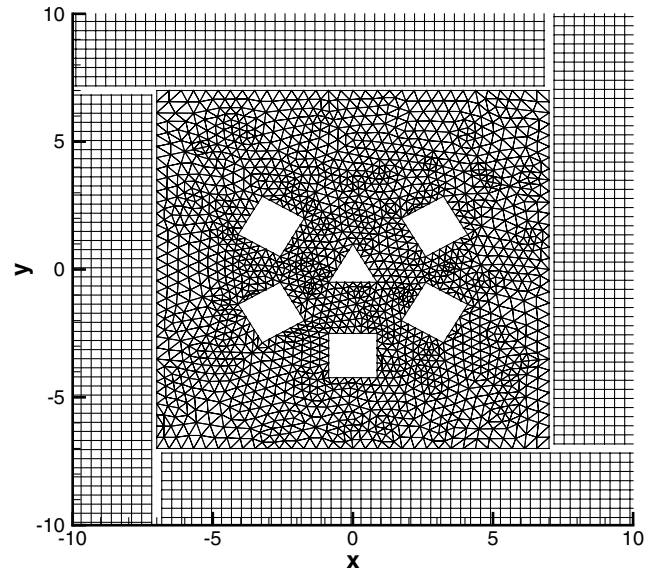

Fig. 48   Domain decomposition for the multiple scattering problem: zoom into the grid.
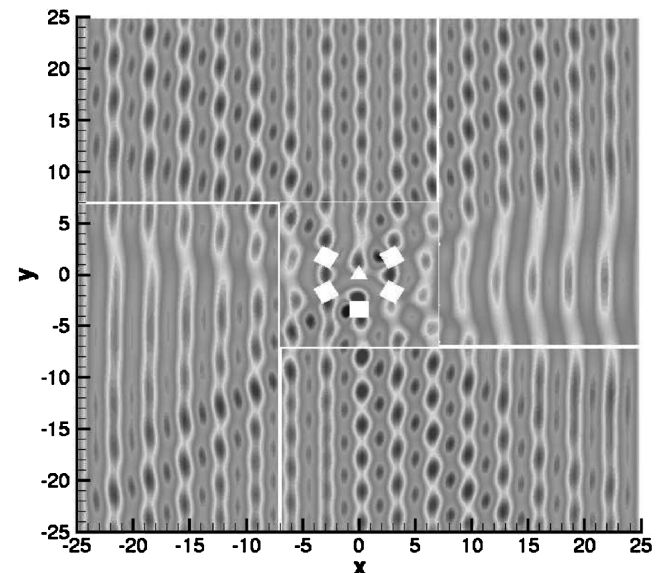

Fig. 49   Instantaneous field of the acoustic pressure fluctuation at $t = 100.0$ **for the multibody scattering problem (** $k = 2$ **).**
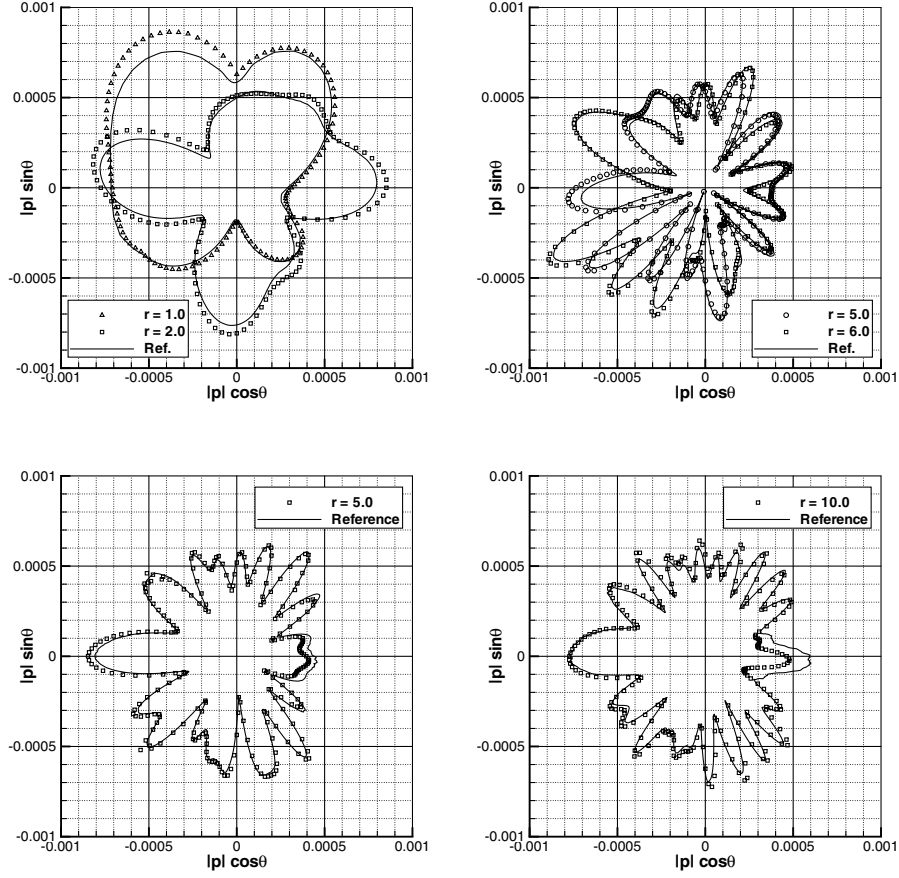
Fig. 50   Directivity patterns of the sound pressure level for the multibody scattering problem ($k = 2$).

problem in a computational domain with extent $[-25; 25] \times [-25; 25]$. The unstructured domain covers the zone $[-7; 7] \times [-7; 7]$. The scatterers are supposed to have perfectly reflecting walls and they are subject to an incident plane wave of wave number $k = 2$. The scatterers consist of one approximately equilateral triangle and five squares, see Figs. 48 and 49. The three nodes of the triangle have the coordinates $(0; 0.5)$, $(-0.866; -0.5)$, and $(0.866; 0.5)$. The lower left corner of the square on the bottom has the coordinate $(-0.866, -4.232)$ and its side length is 1.732. The other four squares are derived from this square by rotation about the origin of ± 60 and ± 120 deg. The configuration of the scatterers is not symmetric which should also be visible later on in the directivity patterns. The unstructured grid contains 3556 elements and the Cartesian blocks have 90×50 cells each, leading to an overall resolution of about 9 PPW. The radiation boundary conditions for the far field are again applied by a sponge layer. We use a 4th order ADER–DG scheme in the unstructured domain and 6th order ADER–FV schemes on the Cartesian blocks.

The reference solution is this time not computed analytically. Instead, we solve the Helmholtz equation for the scattered wave p'_{sc} on a very fine grid with about 32,000 triangles, using the PDE tool of MATLAB. The computational domain is a circle with center $(0/0)$ and radius 25, in the far field, the radiation condition

$$\frac{\partial p'_{sc}}{\partial t} + c_0 \boldsymbol{n} \cdot \nabla p'_{sc} = 0 \qquad (34)$$

is imposed, where $c_0 = 1$ is the speed of sound and $\boldsymbol{n}$ is the outward-pointing normal vector. On the walls we use the boundary condition

$$\frac{\partial p'_{sc}}{\partial n} = -\frac{\partial p'_{in}}{\partial n} \qquad (35)$$

for the scattered wave where the right hand side is known from the incident wave Eq. (31).

The directivity pattern of our numerical simulation is compared with the one obtained with MATLAB in Fig. 50. We can see a very good agreement between both solutions, showing the capability of the domain decomposition approach to tackle this kind of wave propagation problem also in the time domain. Via the coupling of unstructured and Cartesian grids, it is at the same time possible to take into account the presence of obstacles, which might become geometrically even more complicated than the ones shown in this multiple scattering example, as well as computing large domains by switching as fast as possible from unstructured domains to Cartesian domains for the far field.

VI.   Conclusion

A heterogeneous domain decomposition approach for the direct simulation of aeroacoustic problems has been presented. The scheme allows the coupling of different numerical methods, grids, equations, and time steps. It is capable of retaining globally the order of accuracy that is used by the high order methods in the domains. The Cauchy–Kovalevskaja procedure proved to be essential for the coupling of regions with different time steps. Numerical examples showed that the domain decomposition decreases the computational effort of a direct numerical simulation. Especially the wave propagation becomes cheap, as fast methods can be used on Cartesian grids. The extension to 3-D is straightforward with Gauss point coupling. The coupling scheme is currently prepared for parallel computing. All subdomains can be calculated independently with data exchange at the interfaces of adjacent subdomains in each time step. The subdomains can then be divided into MPI partitions.

References

[1] Lighthill, M., "On Sound Generated Aerodynamically—1: General Theory," *Proceedings of the Royal Society of London A*, Vol. 211, No. A1107, 1952, pp. 564–587.

[2] Freund, J., Lele, S., and Moin, P., "Matching of Near/Far-Field

Equation Sets For Direct Computation of Aerodynamic Sound," AIAA Paper 1993-4326, 1993.

[3] Steger, J., Dougherty, F., and Benek, J., "A Chimera Grid Scheme," *Advances in Grid Generation*, edited by K. Ghia, and U. Ghia, Vol. 5, American Society of Mechanical Engineers Fluids Engineering Division, New York, 1983, pp. 59–69.

[4] Meakin, R., "Composite Overset Structured Grids," *Handbook of Grid Generation*, edited by J. Thompson, B. Soni, and N. Weatherill, CRC Press, Boca Raton, FL, 1998.

[5] Toro, E., Millington, R., and Nejad, L., "Towards Very High Order Godunov Schemes," *Godunov Methods: Theory and Applications*, edited by E. Toro, Kluwer/Plenum, New York, 2001, pp. 907–940.

[6] Titarev, V., and Toro, E., "ADER: Arbitrary High Order Godunov Approach," *Journal of Scientific Computing*, Vol. 17, No. 1–4, December 2002, pp. 609–618.

[7] Titarev, V., and Toro, E., "ADER Schemes for Three-Dimensional Nonlinear Hyperbolic Systems," Isaac Newton Institute for Mathematical Sciences Preprint Series, 2003.

[8] Schwartzkopff, T., Munz, C.-D., Toro, E., and Millington, R., "The ADER Approach in 2D," *Discrete Modelling and Discrete Algorithms on Continuum Mechanics*, edited by T. Sonar, Logos Verlag, Berlin, 2001, pp. 207–216.

[9] Schwartzkopff, T., Munz, C.-D., and Toro, E., "ADER: A High Order Approach For Linear Hyperbolic Systems in 2D," *Journal of Scientific Computing*, Vol. 17, No. 1–4, 2002, pp. 231–240.

[10] Schwartzkopff, T., Dumbser, M., and Munz, C.-D., "Fast High Order ADER Schemes for Linear Hyperbolic Equations," *Journal of Computational Physics*, Vol. 197, No. 2, 2004, pp. 532–539.

[11] Schwartzkopff, T., Dumbser, M., and Munz, C.-D., "Fast High Order ADER Schemes for Linear Hyperbolic Equations and Their Numerical Dissipation and Dispersion," Stuttgart University, Tech. Rept. 2003/35, Preprint Series of SFB404, 2003.

[12] Dumbser, M., and Munz, C.-D., "Arbitrary High Order Discontinuous Galerkin Schemes," *Numerical Methods for Hyperbolic and Kinetic Problems*, edited by S. Cordier, T. Goudon, M. Gutnic, and E. Sonnendrucker, IRMA Series in Mathematics and Theoretical Physics, EMS Publishing House, Zürich, Switzerland, 2005, pp. 295–333.

[13] Dumbser, M., and Munz, C.-D., "ADER Discontinuous Galerkin Schemes for Aeroacoustics," *Comptes Rendus Mécanique*, Vol. 333, No. 9, 2005, pp. 683–687.

[14] Dumbser, M., and Munz, C.-D., "Building Blocks for Arbitrary High Order Discontinuous Galerkin Schemes," *Journal of Scientific Computing*, Vol. 27, Nos. 1–3, 2006, pp. 215–230.

[15] Schwartzkopff, T., and Munz, C.-D., "Direct Simulation of Aeroacoustics," *Analysis and Simulation of Multifield Problems*, edited by W. Wendland, and M. Efendiev, Vol. 12, Lecture Notes in Applied and Computational Mechanics, Springer, New York, 2003, pp. 337–342.

[16] Munz, C.-D., and Schwartzkopff, T., "Direct Simulation of Sound Generation and Sound Propagation Using Heterogenous Domain Decomposition," *Proceedings of the Fifth World Congress on Computational Mechanics*, edited by H. A. Mang, F. G. Rammerstorfer, and J. Eberhardsteiner, Vienna University of Technology, Austria, 2002.

[17] Tipler, P., *Physik*, Spektrum Akademischer Verlag, Heidelberg, Germany, 1994.

[18] Schwartzkopff, T., Dumbser, M., and Munz, C.-D., "CAA Using Domain Decomposition and High Order Methods on Structured and Unstructured Meshes," AIAA Paper 2004-2964, 2004.

[19] Tam, C., "Aliasing," *Proceedings of 4th Computational Aeroacoustics (CAA) Workshop on Benchmark Problems*, NASA, CP-2004-212954, 2004.

[20] Tam, C., and Kurbatskii, K., "Multi-Size-Mesh Multi-Time-Step Dispersion-Relation-Preserving Scheme for Multiple-Scales Aeroacoustic Problems," *International Journal of Computational Fluid Dynamics*, Vol. 17, No. 2, 2003, pp. 119–132.

[21] Lax, P., and Wendroff, B., "Systems of Conservation Laws," *Communications on Pure and Applied Mathematics*, Vol. 13, No. 1, 1960, pp. 217–237.

[22] Hirsch, C., *Numerical Computation of Internal and External Flows Vol 1: Fundamentals of Numerical Discretisation*, Wiley, New York, 1988.

[23] Dyson, R., "Technique for Very High Order Nonlinear Simulation and Validation," NASA, Tech. Rept. TM-2001-210985, 2001.

[24] Scott, J., "Single Airfoil Gust Response," *Proceedings of 4th Computational Aeroacoustics (CAA) Workshop on Benchmark Problems*, NASA, CP-2004-212954, 2004.

[25] Scott, J., "Benchmark Solutions for Computational Aeroacoustics (CAA) Code Validation," Institution of Mechanical Engineers Paper 2004-59865, 2004.

[26] Golubev, V., Makbadi, R., and Scott, J., "Numerical Inviscid Analysis of Nonlinear Airfoil Response to Impinging High-Intensity High-Frequency Gust," AIAA Paper 2004-3002, 2004.

[27] Harten, A., Engquist, B., Osher, S., and Chakravarthy, S., "Uniformly High Order Accurate Essentially Nonoscillatory Schemes III," *Journal of Computational Physics*, Vol. 71, No. 2, 1987, pp. 231–303.

[28] Tam, C., "Interface Transmission," *Proceedings of 4th Computational Aeroacoustics (CAA) Workshop on Benchmark Problems*, NASA, CP-2004-212954, 2004.

[29] Morse, P., and Feshbach, H., *Methods of Theoretical Physics*, McGraw–Hill, New York, 1953.

[30] Schwartzkopff, T., and Munz, C.-D., "FastADER: An Arbitrary High Order Scheme for Linear Acoustics," *Proceedings of the 4th Computational Aeroacoustics (CAA) Workshop on Benchmark Problems*, NASA, CP-2004-212954, 2004.

C. Bailly
Associate Editor